

Radio counterparts of gamma-ray sources in the Cygnus region

PAULA BENAGLIA ¹, C. H. ISHWARA-CHANDRA,² JOSEP M. PAREDES ³, HUIB T. INTEMA ^{4,5}, MARCELO E. COLAZO,⁶
AND NATACHA L. ISEQUILLA⁷

¹*Instituto Argentino de Radioastronomía, CONICET-CICPBA-UNLP, CC5 (1897) Villa Elisa, Prov. de Buenos Aires, Argentina*

²*National Centre for Radio Astrophysics, Tata Institute of Fundamental Research, Pune University Campus, Pune, 411007, India*

³*Departament de Física Quàntica i Astrofísica, Institut de Ciències del Cosmos, Universitat de Barcelona, IEEC-UB, Martí i Franquès 1, 08028, Barcelona, Spain*

⁴*International Centre for Radio Astronomy Research, Curtin University, Bentley, WA 6102, Australia*

⁵*Leiden Observatory, Leiden University, Niels Bohrweg 2, 2333 CA Leiden, the Netherlands*

⁶*Comisión Nacional de Actividades Espaciales, Paseo Colón 751 (1063) CABA, Argentina*

⁷*Instituto de Astronomía y Física del Espacio, CONICET-UBA, CC 67, Suc. 28, 1428, Buenos Aires, Argentina*

Submitted to ApJS

ABSTRACT

The view of the gamma-ray universe is being continuously expanded by space high energy (HE) and ground based very-high energy (VHE) observatories. Yet, the angular resolution limitation still precludes a straightforward identification of these gamma-ray emitting sources. Radio observations are an effective tool for searching their possible counterparts at lower energies because the same population of relativistic electrons responsible for radio emission can also produce HE/VHE emission via inverse-Compton scattering. The Cygnus region is crowded by many gamma-ray sources, most of them remaining unidentified. In order to find possible counterparts to unidentified gamma-ray sources, we carried out a deep survey of the Cygnus region using the Giant Metrewave Radio Telescope at 610 MHz and 325 MHz. We did a detailed search for counterparts in the error circle of HE/VHE sources. We report 36 radio sources found in the error ellipse of 15 HE sources, and 11 in those of VHE sources. Eight sources have very steep radio spectral index $\alpha < -1.5$, which are most likely to be pulsars and will be followed up for periodicity search. Such a significant number of pulsar candidates within the error circle of HE/VHE sources prompts fresh look at the energetics and efficacy of pulsars and pulsar wind nebulae in this context.

Keywords: Surveys — Catalogs — Radio continuum emission — Gamma-ray sources — Pulsars — Supernova remnants

1. INTRODUCTION

From the first all-sky gamma-ray surveys and associated catalogs, a large fraction of the discovered sources lacked identification with sources detected along the rest of the electromagnetic spectrum (e.g., [Swanenburg et al. 1981](#)). Since the early days of observations of the gamma-ray sky, emission at these high energies was detected by known and of wide range of sources like blazars, radio galaxies and quasars of the extra-galactic origin and pulsars, supernova remnants and micro-quasars in our Galaxy.

At the GeV energy range, the Energetic Gamma Ray Experiment Telescope aboard the Compton Gamma Ray Observatory, provided a catalog of 271 sources, 170 of which were so-called unidentified gamma-ray sources or UNIDS ([Hartman et al. 1999](#)), with a position accuracy close to half of a degree. In the last decade, the Fermi Large Area Telescope relieved the sky with higher sensitivity and angular resolution (~ 0.1 deg). Its fourth Catalog (4FGL, [Abdollahi et al. 2020](#)) compiles information of five thousand sources above 4σ , and ~ 1300 remain with unknown

nature. The presence of more than one - sometimes many - lower energy sources inside the position error of the high energy (HE: $0.1 \text{ GeV} < E < 100 \text{ GeV}$) sources makes it difficult for the accurate identification of the specific object producing gamma rays.

At very-high energies (VHE: above 100 GeV) a similar percentage of about 22% of unassociated sources is found for VHE sources detected by Cherenkov telescopes. Their distribution is strongly peaked towards the Galactic Plane, thus suggesting an important contribution from Milky Way emitters in this population. Undiscovered pulsars, pulsar wind nebulae or supernova remnants are likely among them. Many studies to find lower energy counterpart's candidates of selected HE/VHE sources have been undertaken during the last years by several authors. As an example, in the field of the unidentified VHE source HESS J1858+020 were found a supernovae remnant interacting with nearby molecular clouds and a few non-thermal sources (Paredes et al. 2014). In the case of HE unidentified sources, we can mention 3FGL J0133.3+5930, where a galactic and an extragalactic objects were proposed as possible counterpart (Martí et al. 2017).

The most energetic phenomena of the Universe give rise to gamma rays: non thermal sources with relativistic particles that interact with fields, matter and radiation. Likewise, the combined ingredients can generate radiation at low radio frequencies, via the synchrotron mechanism. This radio radiation can be measured using radio interferometers, with arcsecond resolution. This superior resolution in the radio band as compared to the HE/VHE facilities will help to precisely localise possible counterparts. Moreover, multi-band observations provide hints on the radiation mechanisms and then on the kind of object that generate the emission measured. As example, Frail et al. (2018) describe, in particular, a method to identify pulsars that can be physically related with unidentified Fermi sources. In short, though the fraction of the counterparts of gamma-ray sources have improved, there are still significant number of sources in the gamma-ray sky which do not have counterpart at any other branch of the electromagnetic spectrum (Abdollahi et al. 2020).

The purpose of this work was to collect evidence and contribute to the identification of discrete HE/VHE sources, by means of radio images at very high angular resolution and very low noise. We focused on a group of such sources detected by the Fermi LAT instrument, and complement it with other sources at TeV energies. We surveyed a highly populated area of the northern sky nearby the Galactic plane at two bands centred at decimetre wavelengths, using the Giant Metrewave Radio Telescope (GMRT). This work is part of a series of studies of the same celestial area in the Cygnus region, mainly the catalog introduced in Benaglia et al. (2020b). The latter lists radio sources at 610 MHz and 325 MHz bands, for flux densities greater or equal to 7σ , where σ is the local rms; see also Ishwara-Chandra et al. (2019); Benaglia et al. (2020a); Isequilla et al. (2020). Here we have studied sources above 3σ . Section 2 describes the observed region including the high-energy sources detected. Section 3 summarizes the data reduction process. In Section 4 we report the results. Section 5 explains the search for counterparts of the radio sources discovered here. A discussion is presented in Section 6, and we conclude in a last Section.

2. THE CYGNUS REGION AND THE GAMMA-RAY SOURCES

The region under study corresponds to the central part of the Cygnus constellation which is relatively nearby and hosts nine OB associations and various rich clusters (Uyaniker et al. 2001; Mahy et al. 2013), see also Reipurth & Schneider (2008) for a review. The region also has many unidentified VHE sources. The observed area covers ~ 20 sq deg, centred at $RA, Dec(J2000) = 20:25:30, 42:00:00$. It encompasses the stellar association of Cyg OB2, and part of Cyg OB8 and OB9, extremely rich in OB stars and with traces of recent star formation (see Figure 2 by Benaglia et al. 2020b).

The Fermi LAT collaboration produced four all-purpose all-sky catalogs, namely First, Second, Third and Four Fermi Gamma-ray LAT (1FGL, 2FGL, 3FGL, 4FGL) catalogs, after the analysis of 0.9, 2, 4 and 8 years of data, respectively (see Abdollahi et al. 2020, and references therein). Besides different data collection periods and slightly different energy ranges (enlarged with date), the analysis software package and the model of the underlying diffuse emission to be subtracted were improved over time. The 4FGL paper covered the range of 0.05 GeV to 1 TeV and detected 5064 point sources above 4σ ; the authors reported that for 1336 they did not find plausible counterparts. The 4FGL catalog has a second release, the LAT 10-year Source Catalogue Data Release 2 (4FGL-DR2)¹.

We selected the point sources of the 3FGL and 4FGL catalogs that lie in the Cygnus region observed at radio bands. There is one source only present at the 4FGL catalog, five sources with 4FGL and 3FGL entries, and seven sources with

¹ https://fermi.gsfc.nasa.gov/ssc/data/access/lat/10yr_catalog/

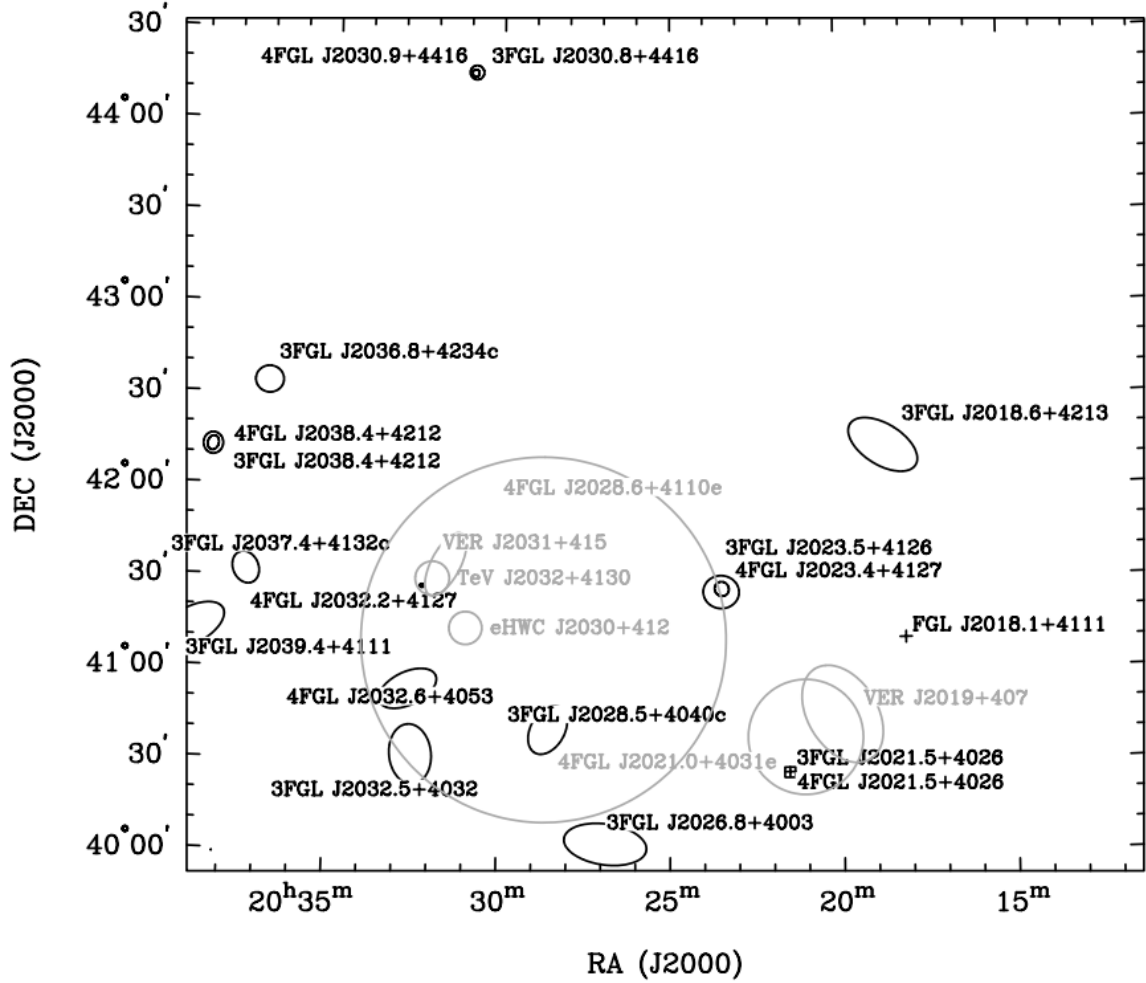


Figure 1. Layout of the HE and VHE sources in the observed region. Discrete GeV (Fermi) sources in black lines; extended GeV and TeV sources in light grey lines.

only 3FGL identification. We added a fourteenth source reported by [Abeysekara et al. \(2018\)](#) by their own reprocessing of Fermi-LAT data. Table 1 lists name, central position, extension, identified or likely associated source/counterpart, reference and variability index from 3FGL and 4FGL catalogs, of the GeV discrete sources considered here. We verified that the 4FGL-DR2 contains the same sources as DR1, and used the error ellipses of DR2. Figure 1 shows the observed area and the location and extension of the studied sources.

2.1. Other gamma-ray sources

Beside the discrete sources detected by the Fermi LAT telescope, there are other gamma-ray sources that lay in the observed region. This second group includes extended sources reported under the Fermi programs, and sources detected at TeV energies, using other instruments, like the Cherenkov instruments High-Energy-Gamma-Ray Astronomy (HEGRA), High Altitude Water Cherenkov (HAWC), and the Very Energetic Radiation Imaging Telescope Array System (VERITAS). Their names, position and extension are given in Table 2 (see also Figure 1).

3. DATA CALIBRATION AND IMAGING

The radio observations used for this investigation were carried out with the GMRT at the bands centred at 325 and 610 MHz, during four campaigns between 2013 and 2017, with a total of 172 hours of observing time. The field of views (FoV) of the GMRT are $81 \pm 4'$ and $43 \pm 3'$ (GMRT Observer's Manual²) at 325 MHz and 610 MHz bands

² www.ncra.tifr.res.in/ncra/gmrt/gmrt-users/observing-help

Table 1. Discrete sources detected by Fermi in the observed Cygnus region

Name	RA_{J2000}	Dec_{J2000}	θ_1, θ_2, PA^a	Assoc. source ^b	Reference	Var.
	(hms)	(dms)	(deg, deg, deg)			index
FGL J2018.1+4111	20:18:07.4	+41:10:44	0.1, 0.1 ^c	—	AB2018	
3FGL J2018.6+4213	20:18:41.89	+42:13:49.4	0.212, 0.112, +57	—	AC2015	35.95
4FGL J2021.5+4026	20:21:32.4	+40:26:40	0.01, 0.01, −31.7	PSR J2021+4026	AB2020	201.76
3FGL J2021.5+4026	20:21:32.5	+40:26:51.68	0.008, 0.008, +17		AC2015	157.71
4FGL J2023.4+4127	20:23:29.1	+41:27:03	0.03, 0.03, +40.0	SSTSL2 J202336.19+	AB2020	11.03
3FGL J2023.5+4126	20:23:30.19	+41:26:01.28	0.098, 0.09, +85	+412527.0	AC2015	48.95
3FGL J2026.8+4003	20:26:51.79	+40:03:09.28	0.228, 0.112, +82	—	AC2015	55.73
3FGL J2028.5+4040c	20:28:32.29	+40:40:37.19	0.143, 0.093, −29	—	AC2015	48.79
4FGL J2030.9+4416	20:30:54.1	+44:16:01	0.02, 0.01, −86.0	PSR J2030+4415	AB2020	3.90
3FGL J2030.8+4416	20:30:51.70	+44:16:13.40	0.039, 0.038, +22		AC2015	36.43
4FGL J2032.2+4127	20:32:15.0	+41:27:32	0.01, 0.01, +59.2	PSR 2032+4127	AB2020	10.65
3FGL J2032.2+4126	20:32:14.29	+41:26:48.8	0.014, 0.014, +17		AC2015	38.32
4FGL J2032.6+4053	20:32:36.6	+40:53:38	0.17, 0.09, −63.4	Cyg X-3	AB2020	67.44
3FGL J2032.5+4032	20:32:30.0	+40:32:05.6	0.165, 0.115, +7	—	AC2015	141.31
3FGL J2036.8+4234c	20:36:53.2	+42:34:05.08	0.077, 0.073, +84	—	AC2015	42.08
3FGL J2037.4+4132c	20:37:24.89	+41:32:02.39	0.09, 0.07, +25	—	AC2015	40.87
4FGL J2038.4+4212	20:38:30.0	+42:12:31	0.05, 0.04, −14.3	—	AB2020	5.52
3FGL J2038.4+4212	20:38:29.89	+42:12:30.6	0.059, 0.054, +14	—	AC2015	45.67
3FGL J2039.4+4111	20:39:24.96	+41:11:52.8	0.2, 0.1, −59	—	AC2015	45.39

NOTE—a: θ_1, θ_2 and PA are the major and minor axis and position angle of the Fermi error ellipse, at 68% for 4FGL sources. b: Identified or likely associated source. c: The authors quote a point source and a PSF of 0.1 deg. AB2018: [Abeysekara et al. \(2018\)](#); AC2015: [Acero et al. \(2015\)](#); AB2020: [Abdollahi et al. \(2020\)](#).

Table 2. Other sources in the observed Cygnus region

Name	RA_{J2000}	Dec_{J2000}	Size	Reference
	(hms)	(dms)	(arcmin)	
VER J2019+407	20:20:04.8	+40:45:36	17.4×11.4	AL2013
4FGL J2021.0+4031e	20:21:04.8	+40:31:12	37.8	AB2020
4FGL J2028.6+4110e	20:28:40.8	+41:10:11.9	180	AB2020
eHWC J2030+412	20:30:57.6	+41:13:48	10.8	ABE2020
VER J2031+415	20:31:33.8	+41:34:38.4	9.5×4	BA2014
TeV J2032+4130	20:32:07	+41:30:30	11.2	AH2002

NOTE—AL2013: [Aliu et al. \(2013\)](#); AB2020: [Abdollahi et al. \(2020\)](#); ABE2020: [Abeysekara et al. \(2020\)](#); BA2014: [Bartoli et al. \(2014\)](#), AH2002: [Aharonian et al. \(2002\)](#).

respectively. According to the FoVs sizes and the region to cover (see Figure 1), we implemented five pointings at 325 MHz and 47 pointings at 610 MHz (45 plus repeating two additional with originally bad data; again, see Figure 2 of [Benaglia et al. 2020b](#)), and taking also into account the requirement to obtain a uniform noise with the minimum amount of pointings. The flux calibrators 3C286 and/or 3C48 were observed at the beginning and at the end of the

observing session. A secondary calibrator 2052+365 was observed for 5 minutes after every 30 mins scan on the target. To minimise the effect of bandwidth smearing, the signal with 33.33 MHz bandwidth was recorded in spectral line mode with 256 channels.

The data was processed with the Source Peeling and Atmospheric Modeling algorithms (Intema 2014), that handle both the calibration and the imaging steps. Full description of acquisition, reduction and imaging of the data is presented with all details in Benaglia et al. (2020b). At imaging, we adopted a robust weighting equal to -1 . The synthesised beams of the final mosaics were $10'' \times 10''$ for the 325 MHz band, and $6'' \times 6''$ at the 610 MHz band. The attained rms values resulted, on average, of up to $0.5 \text{ mJy beam}^{-1}$ and $0.2 \text{ mJy beam}^{-1}$, respectively. The final individual images were mosaicked to get a single image of full region.

Additionally, we also imaged the 325 MHz FoVs, with the Astronomical Imaging Processing System (AIPS) following standard procedures. The data were inspected and flagged manually. The flux density scale for the flux calibrators 3C48 and 3C286 was set using Perley-Butler 2013 scale (Perley & Butler 2013). After the bandpass calibration, the data were averaged keeping in mind to minimise the effect of bandwidth smearing. Multi-facet imaging options were used to correct for w-term due to large field of view. A few rounds of phase-only self-calibration were carried out to correct for phase variations, which has improved the image quality substantially. The primary beam correction was carried out on the final image. The T_{sys} correction due to excess background emission at low radio frequencies in the galactic plane was also applied on the final images.

4. RESULTS

4.1. Radio emission in discrete Fermi sources

We inspected the images at 325 and 610 MHz to search for radio sources above 3σ (rms), that laid in the error ellipses of the GeV sources listed in Table 1. In the process, signals that represented peaks of extended and/or diffuse emission were discarded. For nine discrete Fermi objects, 35 radio sources were found, five of them at only one band.

To derive the radio flux densities, we convolved the 610 MHz image to the synthesised beam of $10''$. We fit Gaussian functions, and verified the value of the integrated flux obtained in that way, by measuring the flux density above the 3σ contour, being σ the local rms. The measurements are given in Table 3.

For the 30 radio sources detected at both bands, we derived the spectral index α , using the convention $S \propto \nu^\alpha$. For the rest, a spectral index upper limit is quoted (see Table 3), except for one with observations only at one band (S35). One must take into account here that the observations at the two radio bands were not simultaneous (see Table 2 of Benaglia et al. 2020b), and that by using the mosaic technique adjacent FoVs limiting areas were averaged.

In what follows, we describe the findings related to each gamma-ray source of Table 1. The individual images of the radio sources are presented in the Appendix.

FGL J2018.1+4111 was discovered by Abeysekara et al. (2018) and reported as a point source of unknown nature, and a PSF at 1 TeV of 0.1 deg. Only one compact radio source at the exact central position of this Fermi source was detected in the radio images at both bands, and named S1; see Figure 2. The spectral index between 325 and 610 MHz resulted in $\alpha = -1.6 \pm 0.2$. Such a steep radio spectrum is a strong indicator that this may be a pulsar.

In the error ellipse of **3FGL J2018.6+4213** we detected eight radio sources at 610 MHz above 3σ emission (sources S2 to S9), and six of them also at 325 MHz (see Figure 3 and Table 3), with flux densities from ~ 1 to almost 500 mJy. One of them is double (S3). Most spectral indices of the six detected at both bands are less or equal to -1 , but one source (S6) exhibited a very steep index of -2.1 ± 0.5 . One possible reason for such a steep radio spectral index is the variability, with the flux variations such that to produce steep spectra. Another possibility is that this is a pulsar candidate. It will be useful to further confirm if the source is variable, if so, this may be a micro-quasar; some of them are VHE sources.

We found no discrete radio sources at the locations of **4FGL J2021.5+4026**, 3FGL J2021.5+4026 or the pulsar PSR J2021+4026, but diffuse and rather strong extended emission (see Figure 4). Probably due to that reason, the 610 MHz FoV (out of the 47 pointings) in which the Fermi source is sitting, resulted with higher noise than average.

The only radio source at the position of **4FGL J2023.4+4127** and 3FGL J2023.5+4126, S10, detected at both radio bands, could be characterized with a spectral index of $+0.2 \pm 0.1$. We note that S10 is inside the 95% error ellipse for this Fermi source; see Figure 5.

Our images covered the northern half (at 325 MHz) and the western half (at 610 MHz) of **3FGL J2026.8+4003**. No radio sources were found, neither at 325 MHz above $0.6 \text{ mJy beam}^{-1}$, nor at 610 MHz FoVs above $1.0 \text{ mJy beam}^{-1}$ of the observed area due to higher noise in this region.

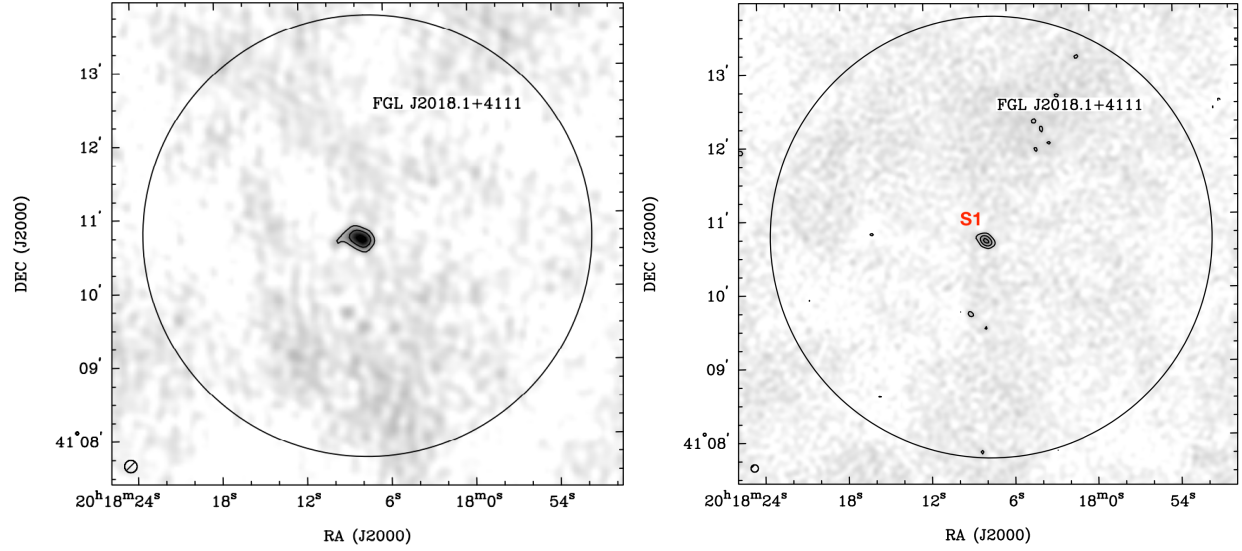


Figure 2. FGL J2018.1+4111. Left: 325 MHz emission; contour levels at -3 , 3 , 7 and 12 in units of σ ($0.25 \text{ mJy beam}^{-1}$). Right: 610 MHz emission; contour levels at -0.3 , 0.3 , 6 and 8.5 in units of σ ($0.1 \text{ mJy beam}^{-1}$). The central source is identified as S1. The synthesized beam is shown in the bottom right corner.

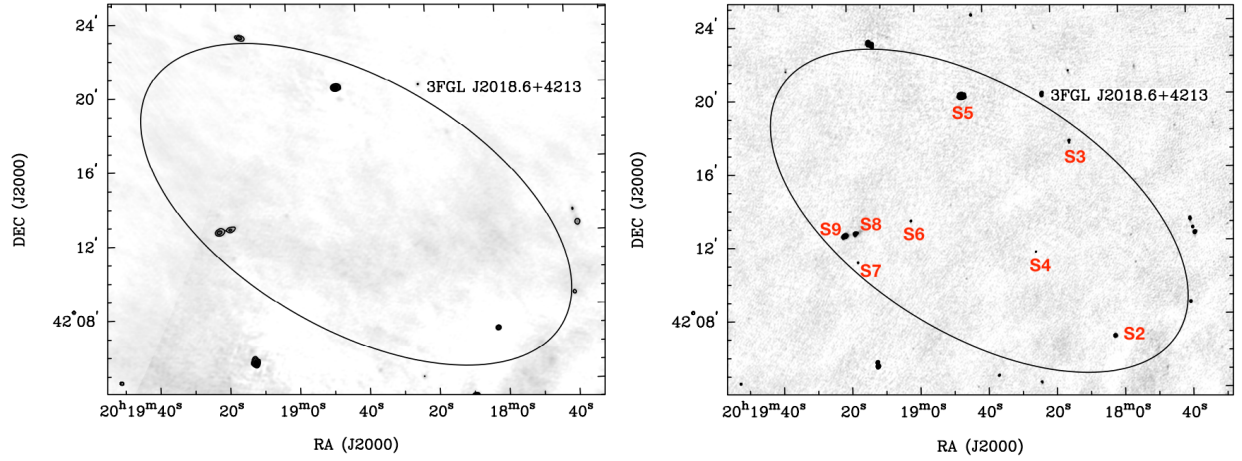


Figure 3. 3FGL J2018.6+4213. Left: 325 MHz emission; contour levels at -3 , 3 and 7 in units of σ ($1.5 \text{ mJy beam}^{-1}$). Right: 610 MHz emission; contour levels at -3 , 3 , 5 and 10 in units of σ ($0.35 \text{ mJy beam}^{-1}$). The radio sources S2 to S9 are identified.

There are two radio sources in the area of **3FGL J2028.5+4040c**. The brighter ($S/N > 350$), S11, double at 610 MHz, presents a spectral index of -1.2 ± 0.1 . The other was detected solely at 610 MHz (see Figure 6 and Table 3).

The area of **4FGL 2030.9+4416** presents weak, diffuse radio emission, probably resolved out due to the weighting scheme adopted in order to outline point sources (see Figure 7). There is an indication that part of that emission could be related to the object PSR J2030+4415 and its wind nebulae (de Vries & Romani 2020). The pulsar wind nebulae is a potential candidate for source of VHE emission (Bednarek & Bartosik 2003). Deeper multi-frequency radio observations are required to confirm this as pulsar wind nebulae which might be powering this VHE source.

In the case of **4FGL J2032.2+4127**, there is a pulsar, namely PSR J2032+4127, which was detected by Fermi (Abdo et al. 2009) in gamma rays and in radio with the Green Bank Telescope (Camilo et al. 2009). Our results showed a radio source coincident with the position of this pulsar, detected at both bands (see Figure 8 and Table 3), and the spectral index derived was -2.0 ± 0.2 . The steep radio spectral index of this known pulsar further strengthens the possibility that other very steep spectrum source may also be pulsars.

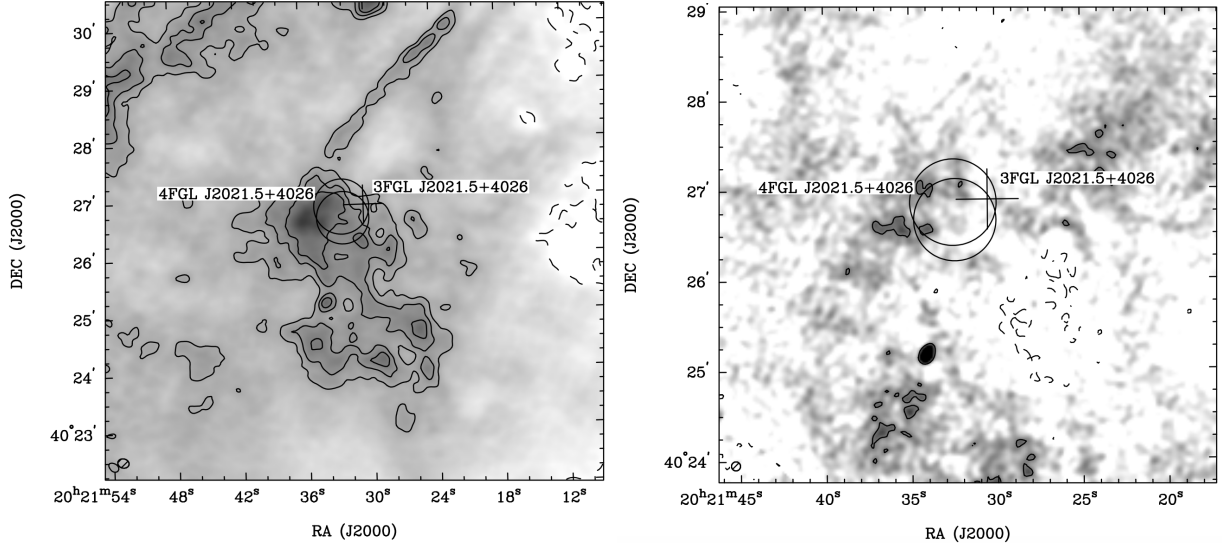


Figure 4. 4FGL J2021.5+4026, represented by the southern circle, at 68%. Left: gray scale emission at 325 MHz with contour levels $-2.5, 2.5, 3.75$ and 5 mJy beam^{-1} . Right: emission at 610 MHz with contour levels at $-1, 1, 3$ and 5 mJy beam^{-1} . The northern circle marks 3FGL J2021.5+4026, and the cross marks the position of the pulsar PSR J2021+4026.

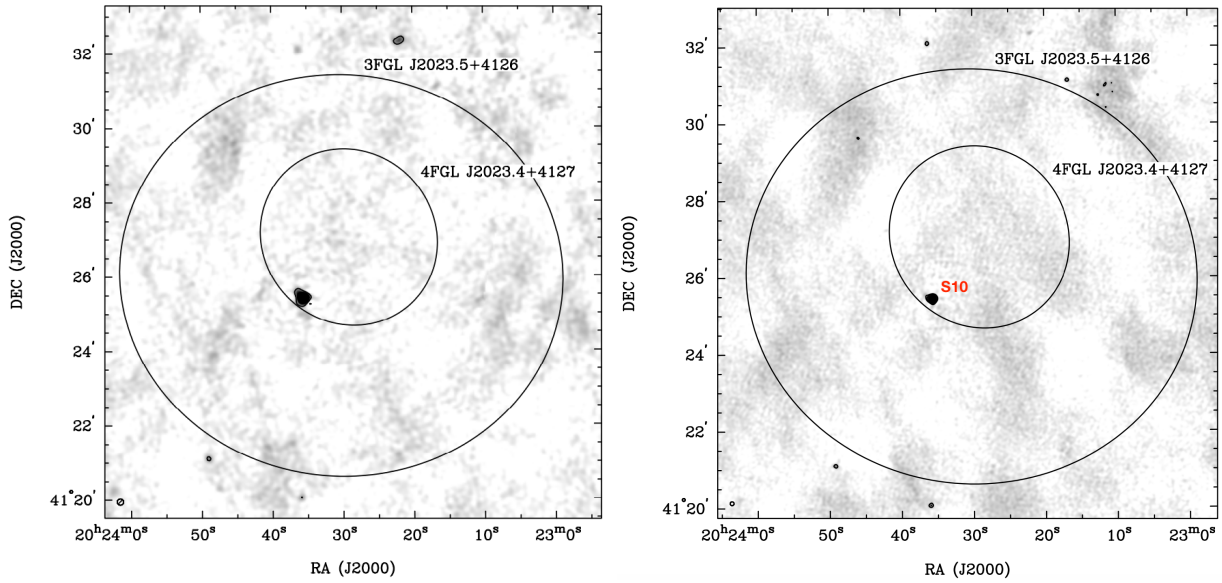


Figure 5. 4FGL J2023.4+4127 at 95%. Left: 325 MHz emission; contour levels at $-3, 3, 10$ and 20 in units of σ ($0.5 \text{ mJy beam}^{-1}$). Right: 610 MHz emission; contour levels $-3, 3, 6$ and 30 in units of σ ($0.2 \text{ mJy beam}^{-1}$). The largest circle represents the position of 3FGL J2023.5+4126. The radio source S10 is identified.

Fourteen radio sources, S14 to S27, were detected inside the ellipse of **4FGL J2032.6+4053**, including one at the position of the micro-quasar Cyg X-3 (S16). Source S26 was only detected at 610 MHz (see Figure 9 and Table 3), and S27 is double. Spectral indices range from -1.6 to $+1.4$.

The source **3FGL J2032.5+4032** overlaps six radio sources, detected at both bands with spectral indices between -1.3 and $+0.5$ (see Figure 10 and Table 3). Two of the radio sources, S32 and S33, are double.

The ellipse of **3FGL J2036.8+4234c** was observed at 610 MHz, and contained no radio sources above a 3σ value of $0.4 \text{ mJy beam}^{-1}$.

The sky area covered by **3FGL J2037.4+4132c** contains one radio source, S34, barely detected at both bands due to diffuse emission present in the field (see Figure 11 and Table 3).

4FGL J2038.4+4212: only observed at 610 MHz, no radio sources above a 3σ value of $0.6 \text{ mJy beam}^{-1}$.

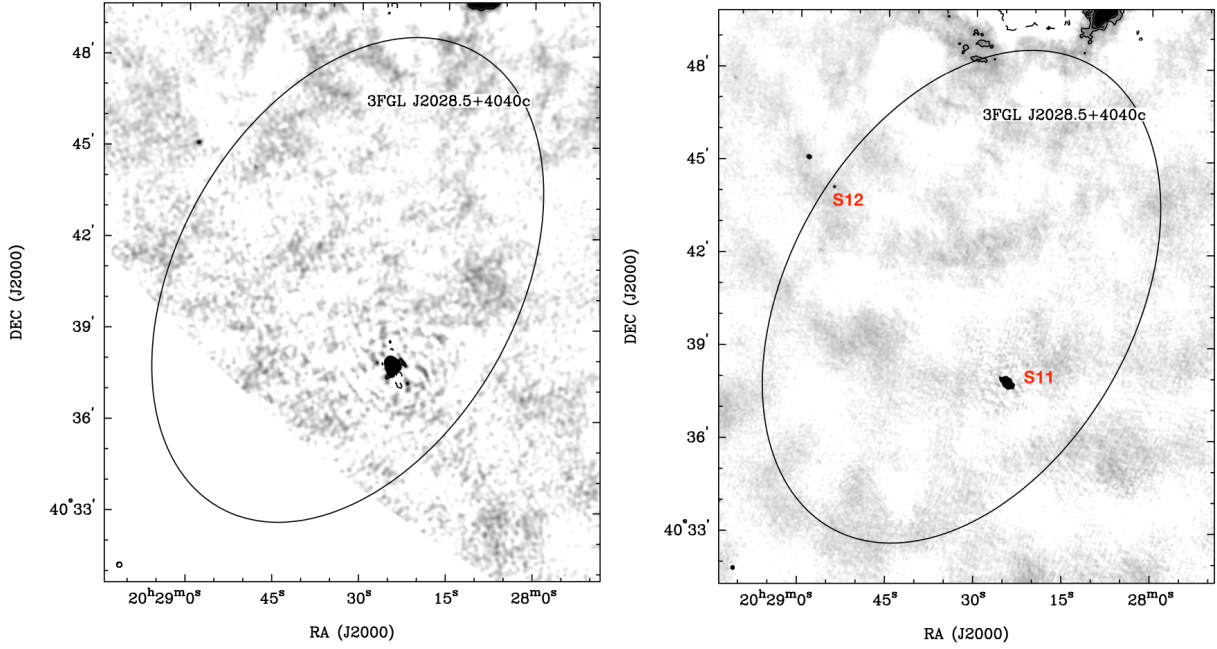


Figure 6. 3FGL J2028.5+4040c. Left: 325 MHz emission; contour levels at -3 , 3 , 5 and 10 in units of σ ($0.9 \text{ mJy beam}^{-1}$). Right: 610 MHz emission; contour levels at -3 , 3 , 5 and 7 in units of σ ($0.3 \text{ mJy beam}^{-1}$). The radio sources S11 and S12 are identified.

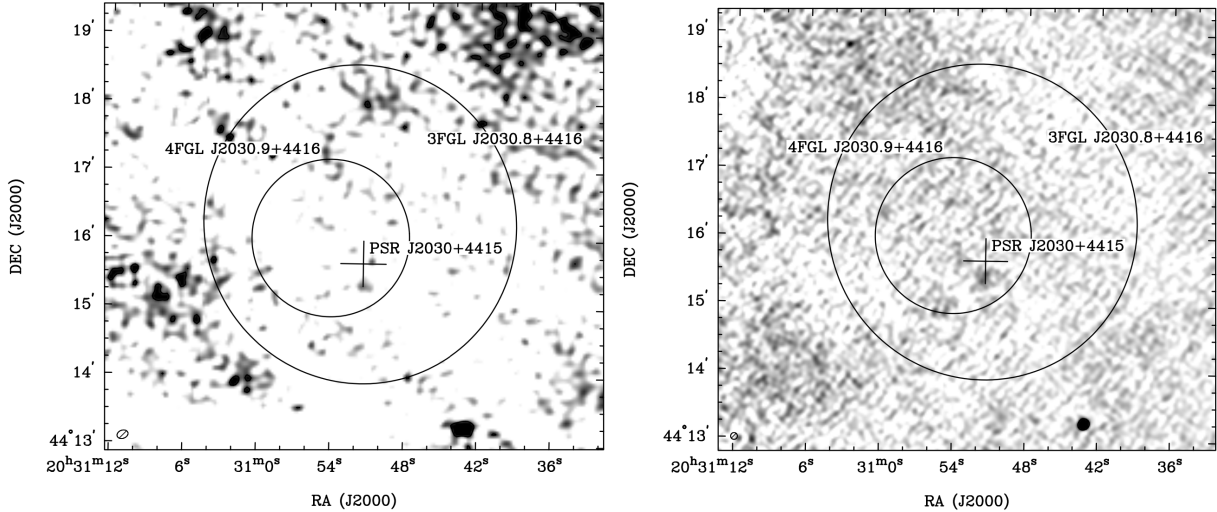


Figure 7. 4FGL J2030.9+4416. Left: 325 MHz emission; contour level at 2 , in units of σ ($0.6 \text{ mJy beam}^{-1}$). Right: 610 MHz emission; contour levels at -2 , and 2 in units of σ ($0.5 \text{ mJy beam}^{-1}$). The position of 3FGL J2030.8+4416 is also represented. The cross marks the position of the pulsar PSR J2030+4415.

The observations at the 325 MHz band partly cover the ellipse of **3FGL J2039.4+4111**, where we detected a radio source tagged as S35, and some extended emission towards the north-east (see Figure 12).

For the gamma-ray sources within which no radio source was detected, we provide in Table 3 the average rms at each observing band.

4.2. Radio emission related to other gamma-ray sources

4FGL J2021.0+4031e is an extended source associated with the supernova remnant Gamma-Cygni (SNR G78.2+2.1). Very recently, the [MAGIC Collaboration et al. \(2020\)](#) studied its energy spectrum and morphology by means of dedicated TeV observations with the MAGIC Imaging Atmospheric Cherenkov telescopes. VERITAS

Table 3. Flux density and spectral index of radio sources detected in the Fermi discrete sources

Gamma-ray source	Radio source		$S_{325\text{MHz}}$	$S_{610\text{MHz}}$	Spectral Index	Remarks
	RA_{J2000}	DEC_{J2000}			α	
	ID	(hh:mm:ss dd:mm:ss)	(mJy)	(mJy)	$(S \propto \nu^\alpha)$	
FGL J2018.1+4111	S1	20:18:07.89 +41:10:41.6	7.5 ± 1.0	2.7 ± 0.2	-1.6 ± 0.2	
3FGL J2018.6+4213	S2	20:18:02.70 +42:06:52.6	28.5 ± 1.0	15.5 ± 0.2	-1.0 ± 0.1	
	S3 *	20:18:15.17 +42:17:32.8	5.8 ± 0.8	4.8 ± 0.3	-0.3 ± 0.3	double source
	S4 *	20:18:25.48 +42:11:31.7	< 2.5	1.2 ± 0.2	> -1.2	
	S5 *	20:18:46.71 +42:20:04.6	400 ± 100	245 ± 5	-0.8 ± 0.4	partially extended
	S6 *	20:19:01.99 +42:13:19.3	7.0 ± 2.0	1.9 ± 0.2	-2.1 ± 0.5	
	S7 *	20:19:17.81 +42:11:07.1	< 2.5	1.3 ± 0.2	> -1.0	
	S8 *	20:19:18.53 +42:12:42.2	53 ± 7	19.5 ± 2.0	-1.6 ± 0.3	overlapping w/ S9?
	S9 *	20:19:22.06 +42:12:32.4	78 ± 6	22 ± 2	-2.0 ± 0.2	overlapping w/ S8?
	—		[0.5]	[0.5]		
4FGL J2021.5+4026	—		[0.5]	[0.5]		
4FGL J2023.4+4127	S10	20:23:35.71 +41:25:26.5	42 ± 3	49.0 ± 0.2	$+0.2 \pm 0.1$	
3FGL J2026.8+4003	—		[0.6]	[1.0]		
3FGL J2028.5+4040c	S11	20:28:24.30 +40:37:49.3	347 ± 9	164 ± 6	-1.2 ± 0.1	double source
	S12 *	20:28:54.10 +40:44:07.8	< 1.5	1.1 ± 0.5	> -0.5	
4FGL J2030.9+4416	—		[0.9]	[0.2]		
4FGL J2032.2+4127	S13	20:32:12.88 +41:27:24.2	2.8 ± 0.2	0.8 ± 0.1	-2.0 ± 0.2	#5 of Pa2007, PSR
4FGL J2032.6+4053	S14	20:31:53.85 +40:55:19.1	5.5 ± 0.3	2.0 ± 0.2	-1.6 ± 0.2	
	S15	20:32:10.30 +40:52:58.2	2.7 ± 0.4	2.8 ± 0.3	$+0.1 \pm 0.3$	
	S16	20:32:25.72 +40:57:27.9	33 ± 2	80 ± 2	$+1.4 \pm 0.1$	Cyg X-3
	S17	20:32:25.10 +40:50:15.7	4.7 ± 0.4	2.0 ± 0.2	-1.4 ± 0.2	
	S18	20:32:34.22 +40:51:30.1	3.7 ± 0.3	1.8 ± 0.1	-1.1 ± 0.2	
	S19	20:32:36.69 +40:55:58.2	11.0 ± 0.4	5.1 ± 0.2	-1.2 ± 0.1	AGN-a (SS2008)
	S20 *	20:32:38.89 +40:55:30.7	2.5 ± 0.3	1.2 ± 0.3	-1.2 ± 0.4	AGN-b (SS2008)
	S21	20:32:39.77 +40:55:06.5	16 ± 1	6.5 ± 0.5	-1.4 ± 0.2	AGN-c (SS2008)
	S22	20:32:38.56 +40:51:47.2	4.7 ± 0.4	2.4 ± 0.1	-1.1 ± 0.2	
	S23	20:32:48.79 +40:48:05.5	11.0 ± 0.6	14.0 ± 0.2	$+0.4 \pm 0.1$	
	S24	20:32:54.70 +40:54:49.3	36.0 ± 1.5	22.5 ± 0.4	-0.7 ± 0.1	
	S25	20:33:07.30 +40:49:15.9	4.2 ± 0.4	2.9 ± 0.3	-0.5 ± 0.2	
	S26 *	20:33:13.31 +40:50:56.4	< 1.2	1.6 ± 0.2	> 0.4	
	S27	20:33:14.80 +40:49:54.0	8.0 ± 0.5	4.2 ± 0.5	-1.0 ± 0.2	double source
	S28 *	20:32:08.40 +40:37:54.5	2.8 ± 0.4	1.9 ± 0.1	-0.6 ± 0.2	
	S29	20:32:29.53 +40:38:50.2	40 ± 1	37.3 ± 0.5	-0.1 ± 0.1	
	S30 *	20:32:34.12 +40:40:00.2	7 ± 1	5.2 ± 1.0	-0.5 ± 0.4	partially extended
	S31	20:32:45.47 +40:39:38.2	28.6 ± 0.5	39.7 ± 0.3	$+0.5 \pm 0.1$	
	S32	20:32:52.33 +40:28:24.0	45 ± 2	20 ± 1	-1.3 ± 0.1	double source
	S33	20:32:55.32 +40:31:31.5	225 ± 4	127 ± 3	-0.9 ± 0.1	double source
3FGL J2036.8+4234c	—		[—]	[0.4]		
3FGL J2037.4+4132c	S34	20:37:26.61 +41:29:24.9	8.0 ± 1.5	5.0 ± 1.5	-0.7 ± 0.6	
4FGL J2038.4+4212	—		[—]	[0.6]		
3FGL J2039.4+4111	S35 *	20:38:56.99 +41:12:09.9	40 ± 5	[—]		

NOTE—The asterisks after the ID indicate radio sources not catalogued in [Benaglia et al. \(2020b\)](#) in at least one band. Numbers in brackets are rms values, and [—] means not observed. Upper limits in flux density correspond to 3σ measured locally. AGNa,b,c (SS2008): components of an AGN discovered by [Sánchez-Sutil et al. \(2008\)](#). Pa2007: [Paredes et al. \(2007\)](#). PSR = PSR J2032+4127 (pulsar).

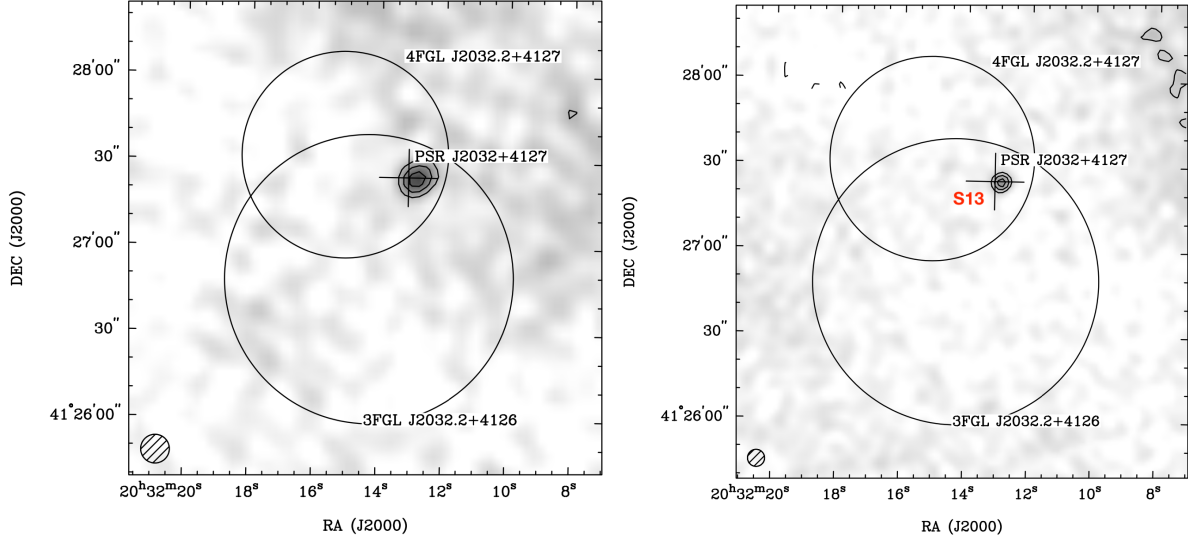


Figure 8. 4FGL J2032.2+4127. Left: 325 MHz emission; contour levels at -3 , 3 , 5 and 7 in units of σ ($0.3 \text{ mJy beam}^{-1}$). Right: 610 MHz emission; contour levels -3 , 3 , 5 , and 7 mJy in units of σ ($0.1 \text{ mJy beam}^{-1}$). The position of 3FGL J2032.2+4126 is also represented. The cross marks the position of the pulsar PSR J2032+4127. The radio source S13 is identified.

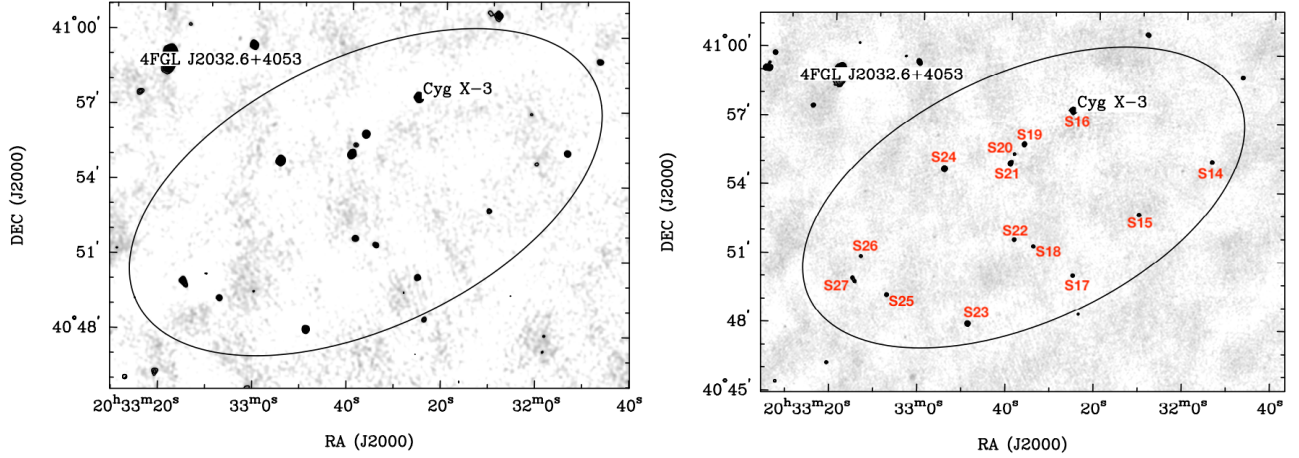


Figure 9. 4FGL J2032.6+4053. Left: 325 MHz emission; contour levels -3 , 3 , 5 , and 7 in units of σ ($0.4 \text{ mJy beam}^{-1}$). Right: 610-MHz emission; contour levels -3 , 3 , 6 , 10 , and 15 in units of σ ($0.2 \text{ mJy beam}^{-1}$). The radio sources S14 to S27 are identified, together with the object Cyg X-3.

reported the discovery of an extended, unidentified source of VHE gamma rays, **VER J2019+407**, lying along the northwestern shell of SNR G78.2+2.1 (Aliu et al. 2013). Enhanced radio emission in this part of the SNR has also been observed at different frequencies, resolutions and sensitivities (Ladouceur & Pineault 2008, and references therein). Our results at 325 MHz also show clearly this enhanced emission but with a good sensitivity and resolution (Fig. 13), despite for 4FGL J2021.0+4031e we found no discrete radio sources in a central region of 0.1 deg in size. A detailed study of the SNR G78.2+2.1 is foreseen and deserves its publication in a future paper, together with the radio sources in this extended field.

We report five radio sources at both observing bands inside the circle that represents **eHWC J2030+412**. One of them, S37, is resolved at 610 MHz. We derive the flux density values at both observing bands by measuring the emission above the 3σ contour (see Table 4 and Fig. 14).

4FGL J2028.6+4110e is a very extended gamma-ray source associated with the Cygnus Cocoon, MGRO J2031+41 and TeV J2032+4130. Due to its extension, we have not done a detailed study of the many sources in the area. A list of the sources detected at radio with more than 7σ can be found in the catalog of Benaglia et al. (2020b). Here we

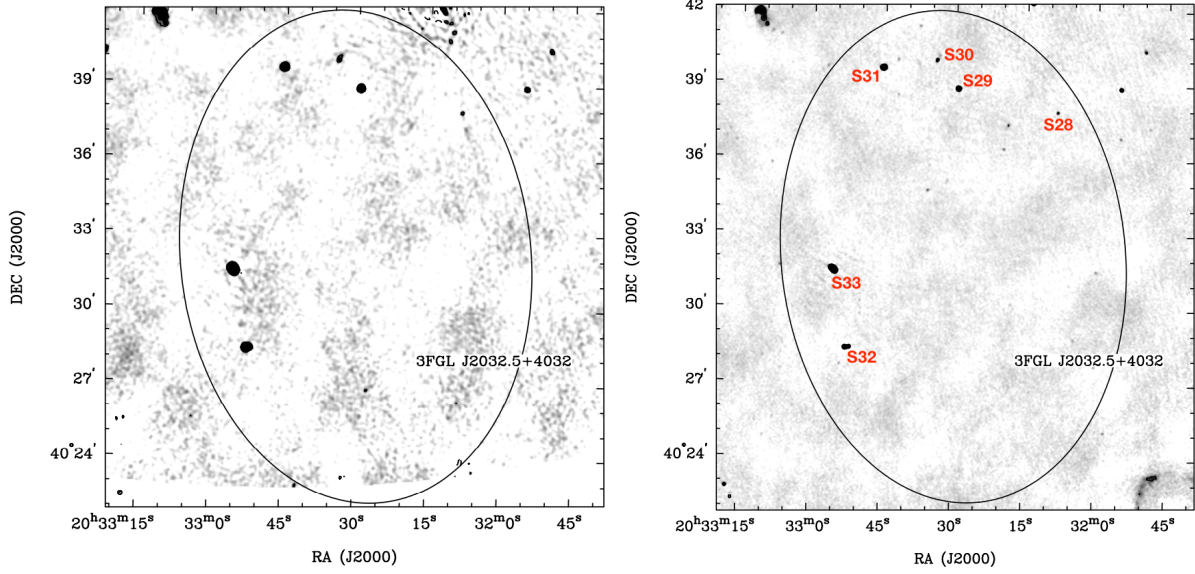


Figure 10. 3FGL J2032.5+4032. Left: 325 MHz emission; contour levels -3 , 3 and 5 in units of σ ($0.7 \text{ mJy beam}^{-1}$). Right: 610-MHz emission; contour levels -3 , 3 and 5 in units of σ ($0.45 \text{ mJy beam}^{-1}$). The radio sources S28 to S33 are identified.

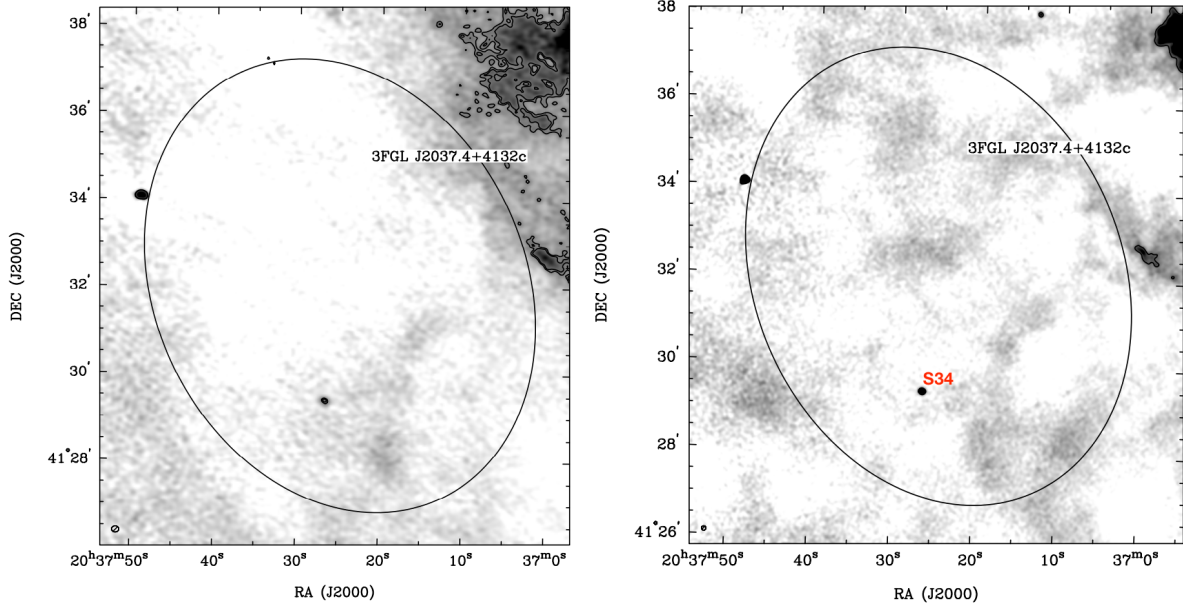


Figure 11. 3FGL J2037.4+4132c. Left: 325 MHz emission; contour levels of 5 and 10 in units of σ (1 mJy beam^{-1}). Right: 610 MHz emission; contour levels -3 , 3 and 5 in units of σ ($0.4 \text{ mJy beam}^{-1}$). The radio source S34 is identified.

only show a radio source at the very center of the Fermi source, S41, with very steep radio spectra (see Table 4), that turns it a strong candidate for pulsar.

TeV J2032+4130 was detected by HEGRA (Aharonian et al. 2002, 2005), and that was the first source discovered of a population of extended TeV sources without low-frequency counterparts. The discovery was later confirmed by MAGIC (Albert et al. 2008) and VERITAS (Aliu et al. 2014), as source **VER J2031+415**. The pulsar PSR J2032+4127, detected by Fermi (4FGL J2032.2+4127), and S13 here, is within the field of TeV J2032+4130. The area had been observed with the GMRT at 610 MHz by Paredes et al. (2007). Apart from the detection of PSR J2032+4127 at 325 and 610 MHz, we have detected other sources (see Table 4 and Fig. 15) in the areas limited by the HEGRA, MAGIC and VERITAS; one is double (S42). Maybe one of them could contribute additionally to the

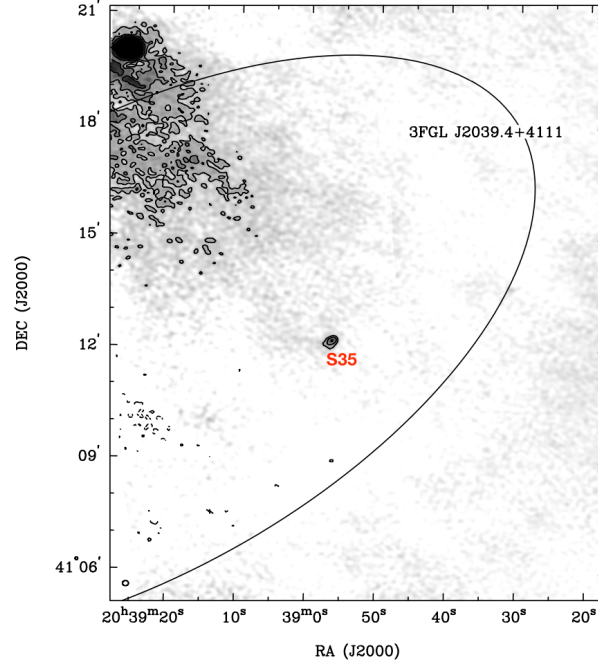


Figure 12. 3FGL J2039.4+4111. 325 MHz emission; contour levels $-3, 3, 5$ and 8 in units of σ ($1.6 \text{ mJy beam}^{-1}$). The radio source S35 is identified.

Table 4. Flux density and spectral index of radio sources detected in extended and/or TeV γ -ray sources

Gamma-ray	Radio source		$S_{325\text{MHz}}$	$S_{610\text{MHz}}$	Spectral Index	Remarks	
source		RA_{J2000}	DEC_{J2000}		α		
	ID	(hh:mm:ss)	(dd:mm:ss)	(mJy)	(mJy)	$(S \propto \nu^\alpha)$	
eHWC J2030+412	S36 *	20:30:42.92	+41:13:28.1	2.5±0.2	1.7±0.4	−0.6 ± 0.4	
	S37	20:31:07.66	+41:14:07.3	7.0±0.3	5.4±0.3	−0.4 ± 0.1	Ma2007, triple source
	S38 *	20:31:10.16	+41:16:48.9	1.5±0.1	1.1±0.1	−0.6 ± 0.2	
	S39 *	20:31:12.93	+41:17:07.3	1.4±0.2	0.5±0.1	−1.6 ± 0.4	Ma2007
	S40	20:31:14.93	+41:11:25.7	5.1±0.5	6.4±0.2	+0.4 ± 0.2	Ma2007
4FGL J2028.6+4110e	S41 *	20:31:09.70	+42:30:24.6	5.9±1.0	1.9±0.2	−1.8 ± 0.3	
VER J2031+415	S42	20:31:12.37	+41:39:03.9	84.7±2.0	40.0±2.0	−1.2 ± 0.1	Ma2007, double source
	S43 *	20:31:18.83	+41:34:43.9	1.9±0.3	0.6±0.2	−1.8 ± 0.6	Ma2007
	S44 *	20:31:20.71	+41:34:59.3	1.0±0.2	1.0±0.2	+0.0 ± 0.5	Ma2007
TeV J2032+4130	S45 *	20:31:49.69	+41:32:08.9	1.4±0.4	0.4±0.1	−2.0 ± 0.6	#2 of Pa2007
	S46 *	20:31:51.59	+41:31:18.6	2.1±0.2	0.8±0.1	−1.5 ± 0.3	#3 of Pa2007
	S47 *	20:32:16.06	+41:30:56.0	0.8±0.2	0.6±0.1	−0.5 ± 0.5	#6 of Pa2007

NOTE—Asterisks as in Table 3. S45 and S46 correspond to the region where the error ellipses of the two last VHE sources overlap. Ma2007: Martí et al. (2007), Pa2007: Paredes et al. (2007). TeV J2032+4130 contains 4FGL J2032+4127, and the radio source S13 (see Table 3 and also Pa2007).

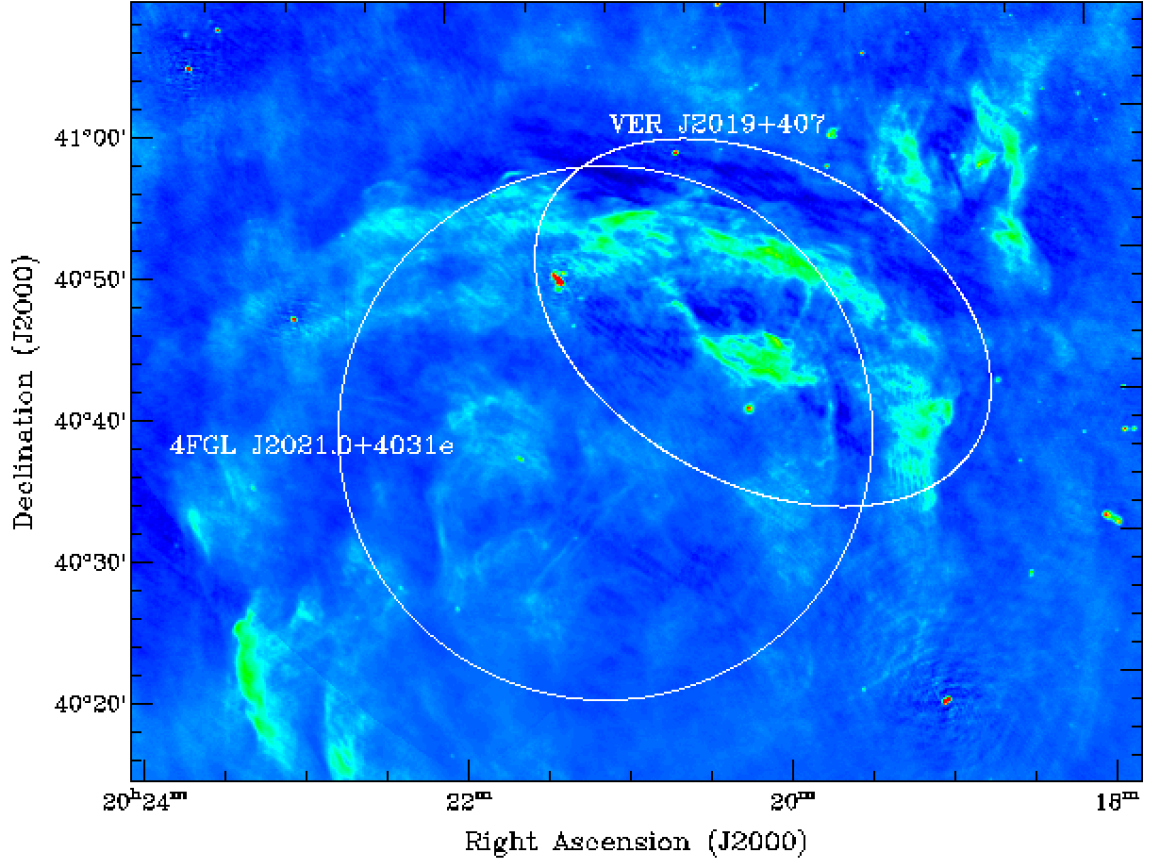


Figure 13. 325 MHz radio image of the SNR Gamma-Cygni (G78.2+2.1) with the overlaid contours of the Fermi source 4FGL J2021.0+4031e and the VERITAS source VER J2019+407. The color scale interval shown is $(-48, +83)$ mJy beam $^{-1}$, to outline weaker features.

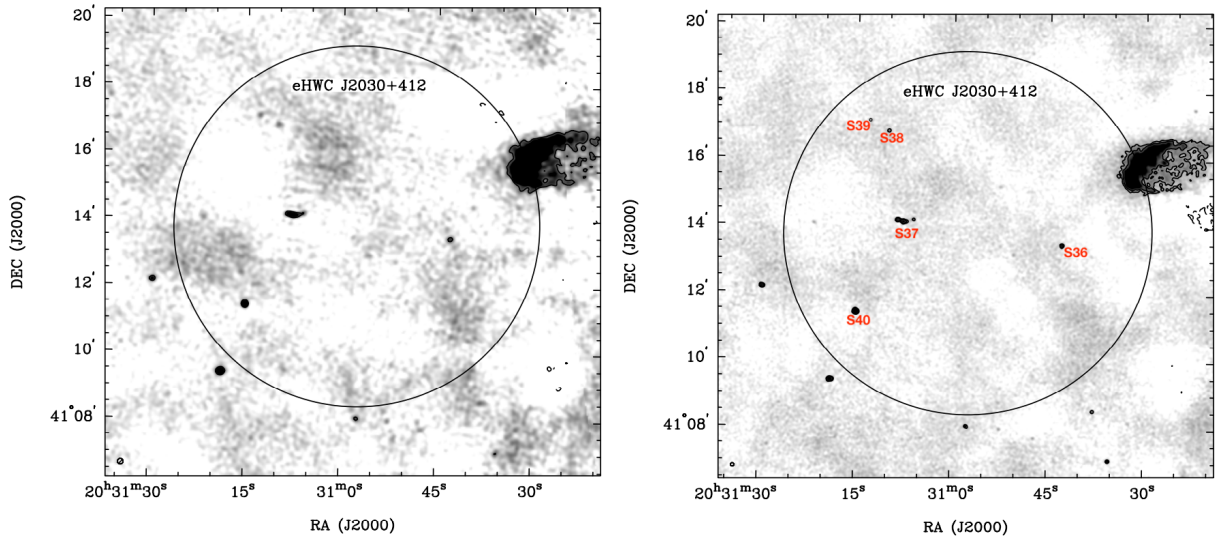


Figure 14. eHWC J2030+412. Left: 325 MHz emission; contour levels $-3, 3, 5, 10$ and 20 in units of σ (0.5 mJy beam $^{-1}$). Right: 610-MHz emission; contour levels $-3, 3, 5, 10$ and 20 in units of σ (0.17 mJy beam $^{-1}$). The radio sources S36 to S40 are identified.

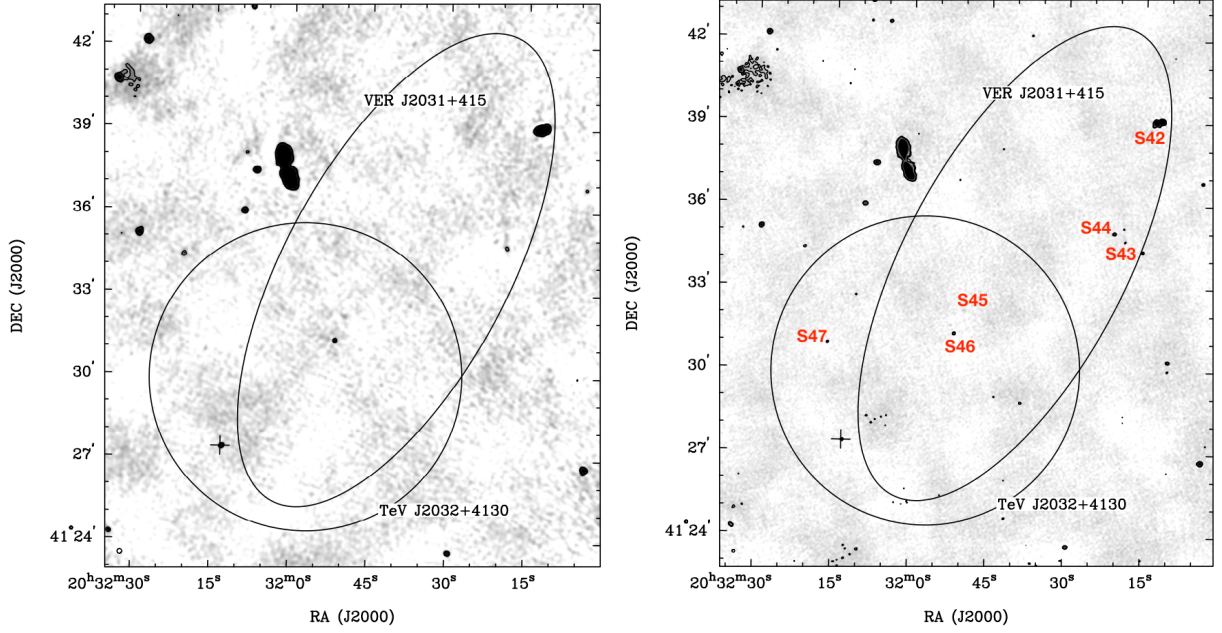


Figure 15. TeV J2032+4130 and VER J2031+415. Left: 325 MHz emission; contour levels -3 , 3 and 4.5 in units of σ ($0.4 \text{ mJy beam}^{-1}$). Right: 610-MHz emission; contour levels -3 , 3 and 4.5 in units of σ ($0.12 \text{ mJy beam}^{-1}$). The radio sources S42 to S47 are identified. The cross is the pulsar PSR 2032+4127 (and S13).

emission of this extended gamma-ray source because it is not clear if the pulsar alone can be responsible of the full emission.

The search for radio counterparts related to sources of Table 2 provided twelve more candidates (S36 to S47), presented in Table 4, totalling then 47 radio sources found (see the figures in the Appendix).

5. COUNTERPARTS AT OTHER SPECTRAL RANGES

In order to obtain additional information from the radio sources, we searched several large catalogs in the literature. These are listed in Table 5 and offer results collected with instruments working from radio to X-ray bands. Regarding the search of radio counterparts on catalogs of massive, early-type stars, involving the same observations and images used here, see Benaglia et al. (2020a).

In the case of the 2MASS, WISE and Spitzer-SSCSL lists (Cutri et al. 2003; Cutri & al. 2012; Capak et al. 2013), we found that a wealth of objects permeate the fields of the radio sources S1 to S47, and in the vast majority of the cases, their nature is not determined. Since the objects bright at infrared are usually thermal emitters, and we are interested here on non-thermal sources, we considered the 2MASS, WISE and SSCSL sources that overlap the radio sources only in the cases for which the nature of the IR source was known.

Table 6 summarizes the results of the search for counterparts in the mentioned catalogs, to the radio sources S1 to S47.

The individual figures of the radio sources S1 to S47 (Sect. Appendix) show the positions of the counterparts found as well. The membership of the counterparts to a given catalog are shown with labels: C1 with “TGSS”, C2 with “WENSS”, C3 with “1.4GHz”, C4 with “NVSS”, C6 with “87GHz”, C10 with “XMM”, and C11 with “XCHA”. C7 sources are represented with small boxes, C8 sources with small crosses and C9 sources with small circles.

We also compared the radio sources detected here with those listed in Benaglia et al. (2020b), a catalog of ~ 3800 sources at the same Cygnus region carried out with the Giant Metrewave Radio Telescope at 325 and 610 MHz. The article provides the list of sources detected in the SPAM-generated mosaics (see Section 3), with integrated flux densities above 7σ (local rms). Radio sources with an asterisk in Table 3 are presented, at least at one band, here for the first time.

6. DISCUSSION

6.1. On the catalogs search results

Table 5. Catalogs used to look for counterparts to the radio sources S1 to S47

ID	Name	Reference	Associated symbol ^a
C1	TGSS Alternative Data Release	Intema et al. (2017)	25''-side square
C2	The Westerbork Northern Sky Survey	Rengelink et al. (1997)	35''-radius circle
C3	Small-diameter radio sources catalogue	Zoonematkermani et al. (1990)	2'' × 3'' ellipse
C4	NRAO VLA Sky Survey	Condon et al. (1998)	25''-radius circle
C5	The MIT-Green Bank 5GHz Survey	Bennett et al. (1986)	
C6	87GB Catalog of radio sources	Gregory & Condon (1991)	3'' × 2'' ellipse
C7	2MASS All-Sky Catalog of Point Sources	Cutri et al. (2003)	small square
C8	Spitzer Science Center Source List	Capak et al. (2013)	small cross
C9	WISE All-Sky Data Release	Cutri & al. (2012)	small circle
C10	3XMM-Newton Serendipitous Source Catalogue-DR6	XMM-SSC, 2016	small filled circle
C11	CHANDRA ACIS Survey of X-Ray Point Sources	Wang et al. (2016)	small filled circle
C12	ATNF Pulsar Catalog	Manchester et al. (2005)	

NOTE—a: symbol used to represent the source in Figures 17, 18, 19, and 20.

Table 6. Sources in catalogs of Tables 3 and 4 positionally coincident with the radio sources S1 to S47

Source	Object name	Catalog ^a	Type	Other reference
S5	NVSS J201847+422010	C1,C2,C4	radio source	
S10	WISEA J202335.82+412523.5	C9	YSO	Kryukova et al. (2014)
S11	NVSS J202824+403751	C1,C2,C4	radio source	Wendker et al. (1991)
S13	PSR J2032+4127	C10,C11,C12	pulsar	Abdo et al. (2009)
S16	Cyg X-3	C3,C4,C6,C10,C11	HMXB	Sánchez-Sutil et al. (2008)
S19	2XMM J203237.5+405557	C10	X-ray source	
S23	CXOGSG J203248.8+404804	C11	X-ray source	
S27	2MASS J20331489+4049096	C7	star	
S29	G079.602+0.506	C3	radio source	Wendker et al. (1991)
S31	MWC 349	C3,C4	OB star(s)	Cohen et al. (1985)
S33	NVSS J203254+403128	C2,C4	radio source	Wendker et al. (1991)
S46	XMM J203151.8+413118	C10,C11	X-ray source	

NOTE—a: We included sources of C7, C8 and C9 only if their nature is known.

At the position of **S5** lies the known sources NVSS J201847+422010, WENSS B2017.0+4210 and TGSS J201846.6+422010. Their integrated flux densities, at 1400, 325, and 150 MHz, are 95.8 ± 3.5 , 323 and 620.6 ± 84.6 mJy (see Fig. 17 and corresponding symbols according to Table 5). The Gaussian fit to S5 with our GMRT data resulted in a discrete source, among errors. Regardless the different angular resolutions used in the various measurements collected, S5 clearly stands as a non-thermal source with a spectral index close to -1 , if the flux values at 325 MHz are averaged.

[Kryukova et al. \(2014\)](#) reported a Young Stellar Object (J202335.81+412523.53) at the location of **S10**. It showed a spectral index of $+0.2 \pm 0.1$. Although there are studies of such objects and related types that predict, under certain conditions, gamma-ray emission from them, this is expected for those characterized by non-thermal spectral indices (see, for instance, [Bosch-Ramon et al. 2010](#)). Thus, we do not expect high-energy contribution from this source (Fig. 17).

S11 is another source with radio counterparts, as NVSS J202824+403751, WENSS B2026.6+4027 and TGSS J202824.3+403749; the integrated flux densities are 12.8 ± 0.7 , 218 and 392.8 ± 44.2 mJy, respectively (see Fig. 17). Wendker et al. (1991) reported at the same position the source 19P06, with a flux at 1400 MHz of 64 ± 3 mJy, and Taylor et al. (1996), at 327 MHz, WSRT 2026+4027 with 126 ± 7 mJy. A mean spectral index of -0.8 is obtained considering all measurements.

S13 is associated with the gamma-ray pulsar PSR J2032+4127. This source was first detected, with a flux density of 0.7 ± 0.2 mJy, in a search of radio sources carried out by GMRT at 610 MHz in the field of the unidentified gamma-ray source TeV J2032+4130 (Paredes et al. 2007), measurement in full agreement with the flux reported here. XMM J203213.2+412723 (C10) and CHA J203213.1+412722 (C11) are other overlapping sources (see Fig. 18). The object, a binary system composed by a pulsar and a Be star, has been widely studied (see for instance Chernyakova et al. 2019, and references therein), and is listed in the 4FGL catalog as the counterpart to Fermi source 4FGL J2032.2+4127. S13 is the only radio source detected by us in the Fermi ellipse. The spectral index derived here fits well for what is expected for pulsars.

The source **S16** agrees with the coordinates of the micro-quasar/High Mass X-ray Binary Cyg X-3, also a well known system, and associated with the source 4FGL J2032.6+4053. But contrary to the previous case, S16 is just one of the fourteen radio sources detected in the area of the Fermi source (see Fig. 18). Sánchez-Sutil et al. (2008) studied radio emission around this object at 2 and 6 cm, finding an extended diffuse radio structure south to Cyg X-3, and suggesting non-thermal emission. Our image at 325 MHz of the same area, built with a robust weighting of 0.0, showed such feature (see Fig. 16). At the position of S16, the catalog search yielded radio sources at 1.4 GHz (NVSS J203225+405728 of C4; G079.846+0.700 of C3), and at 87 GHz (J203037.0+404726, C6), five C10 sources and one C11 source (symbols as per Table 5).

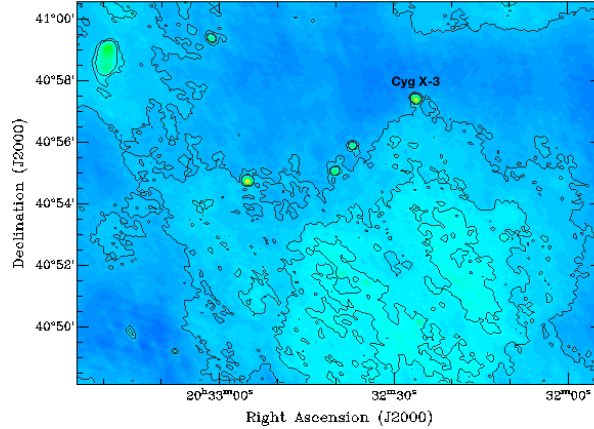


Figure 16. Image at 325 MHz of the Cyg X-3 area, outlying diffuse extended emission. Color scale interval shown: $(-51.3, +70.5)$ mJy beam $^{-1}$; contour levels: 0.3, 1.8 and 3.0 mJy beam $^{-1}$.

Two X-ray sources are positionally coincident with **S19** (XMM J203236.1+405603 and XMM J203237.5+405558). Sources S19, 20 and 21 have been identified by Sánchez-Sutil et al. (2008) as parts of an AGN. The spectral indices derived here confirm that result.

S23 is another radio source with an X-ray counterpart, CXOGSG J203248.8+404804, detected by means of CHANDRA observations.

A star identified as 2MASS J20331489+404804 is reported at the location of **S27**.

The radio source **S29** shows a counterpart detected with the VLA at 1.4 GHz, G079.602+0.506 (C3), and also overlaps the source 19P18 (Wendker et al. 1991).

S31 is identified with the source MWC 349, proposed to be an OB+OB system. It is also listed as a C4 source (NVSS J203245+403938). The radio spectrum of this stellar system is analyzed in Benaglia et al. (2020a) (see references therein).

At the position of **S33** there are NVSS J203254+403128 (flux density of 23.1 ± 0.9 mJy), and WENSS B2031.1+4021 (integrated flux of 102 mJy) sources, and Wendker et al. (1991) reported the source 19P22. The global spectral index remains negative.

In the case of **S37**, we found a source at 610 MHz resolved in three components. Previous work on this area was carried out by [Martí et al. \(2007\)](#) (see Fig. 20 of the Appendix). The authors discovered, with the GMRT at the same frequency band, two sources at the position of S37, with coordinates in agreement between error bars with the two brighter maxima of S37. They reported flux densities of 0.95 ± 0.11 mJy, and 0.86 ± 0.11 mJy. We measure a slightly larger flux above the 3σ contour corresponding to the position of the 2007 sources: 4.3 ± 0.1 mJy, although two of the S27 maxima correspond to the detection by [Martí et al. \(2007\)](#).

S39, **S40**, **S42**, **S43** and **S44** were discovered by [Martí et al. \(2007\)](#) at 610 MHz, with flux densities of 0.53 ± 0.11 , 3.56 ± 0.11 , $(12.06 + 15.51) \pm 0.11$, 0.57 ± 0.11 mJy and 0.97 ± 0.11 , respectively. Except in the case of S40, their values for the point sources agree very well with those reported here.

The source S42 was also detected by [Taylor et al. \(1996\)](#) as J2029+4129, with a flux density of 51 ± 3 mJy (Fig. 20).

S46 was detected at X-rays (XMM J203151.8+413118 of C10, and CHA J203151.8+413119 of C11, Fig. 20).

[Paredes et al. \(2007\)](#) reported the detection at 610 MHz of **S45**, **S46** and **S47**, with flux densities of 0.50 ± 0.16 , 1.75 ± 0.19 mJy and 0.77 ± 0.18 mJy. The values for S45 and S47 are coincident with ours. For S46, the flux seems to have drop to a half in the decade between the two observations (~ 2006 – 2016) and the spectral index is now more steeper (-1.5 ± 0.3) than before (-0.47 ± 0.03), although in both cases is non-thermal. The difference between the flux densities of S40 and S46 can be ascribed to some kind of variability, a common phenomenon in this type of MHz sources, and could explain the different spectral indices found.

6.2. Radio sources with steep spectral indices

Among the 47 radio sources, there is a group that shows very negative α values. Such steep spectral indices are usually associated with pulsars. [Bates et al. \(2013\)](#) performed a detailed study on the spectral distribution of this type of sources. They analyzed the spectral indices of ~ 1300 pulsars at the radio range, and combined techniques of population synthesis and likelihood analyses to find the spectral index distribution. They modeled the survey results with a Gaussian function in spectral index distribution with the mean at $\alpha = -1.4 \pm 1$.

Later on, [Frail et al. \(2016, 2018\)](#) devised a method to pinpoint pulsar candidates, taking into account the spectral index and the compactness C of radio sources at low radio frequencies. The authors defined C as the flux density over the peak brightness of the radio source. They studied TGSS-ADR1 together with NVSS sources, and showed that in the αC plane, the distribution for typical radio sources differed significantly from that of pulsars (see their Figure 1). The mean spectral index resulted in $\alpha = -0.73$ for the first group, and ~ -1.8 in the case of pulsars (see also [Intema et al. 2017](#)). Pulsar (candidates) share the extreme index values with luminous high-redshift galaxies ([Frail et al. 2016](#)), although it is not expected to receive VHE gamma-rays from the latter because absorption ([Biteau & Williams 2015](#)). [Frail et al. \(2018\)](#) characterized promising pulsar candidates as having both $\alpha \leq -1.5$ and $C \leq 1.5$. The method was applied to TGSS-ADR1 and NVSS sources in the error ellipses of Fermi LAT UNIDs of 3FGL. Out of sixteen pulsar candidates identified, with follow-up continuum observations and timing, they found six ms pulsars and one normal pulsar. They considered that propagation effects through the ISM for instance, could prevent the pulsars to pop up during periodicity searches. The pulsed radio beams can even point off the line of sight ([Camilo et al. 2012](#)).

Table 7 contains eleven sources with $\alpha \leq -1.5$, being one of them S13, the known pulsar PSR 2032+4127 that is associated to 4FGL J2032.2+4127. Regarding their compact factor, in nine out of the eleven cases it remains lower or close to 1.5, another feature in common with known pulsars. And two radio sources, S8 and S9, have very steep spectral indices with larger compact factors, and the overall morphology resembles an AGN-like double source; all points to an extragalactic origin.

Leaving aside the resolved sources S8 and S9, the radio sources of Table 7 overlap infrared sources, that need to be studied as possible stars related to a pulsar. Their radio fluxes measured in this work are of the same order as those reported by [Frail et al. \(2016\)](#). None of them presented a 1.4 GHz counterpart (catalog C3).

According to [Acero et al. \(2015\)](#), a Fermi source with variability index greater than 73 is considered as probably variable. The last column of Table 1 shows that the variability indices of the Fermi sources for which the steepest spectral indices were measured, are below the value mentioned above. On the contrary, for the two Fermi sources showing values larger than 73, either we did not detect radio counterparts (4FGL J2021.5+4026) or the detected ones showed spectral indices ≥ -1.3 (3FGL J2032.5+4032), thus no pulsar candidates.

Finally, it is worth noticing that there are seven sources in Tables 3 and 4 showing spectral indices between -1.5 and -1.2 . Three correspond to a previously proposed AGN (S19, S20, S21, [Sánchez-Sutil et al. 2008](#)). Another three show

Table 7. Radio sources with very steep spectral index

HE/VHE source	ID	α	C -factor ^a
FGL J2018.1+4111	S1	-1.6 ± 0.2	1.7
3FGL J2018.6+4213	S6	-2.1 ± 0.5	1.1
	S8	-1.6 ± 0.3	3.4
	S9	-2.0 ± 0.2	4.9
4FGL J2032.2+4127	S13	-2.0 ± 0.2	1.0
4FGL J2032.6+4053	S14	-1.6 ± 0.2	1.2
eHWC J2030+412	S39	-1.6 ± 0.4	1.1
4FGL J2028.6+4110e	S41	-1.8 ± 0.3	1.0
VER J2031+415	S43	-1.8 ± 0.6	1.1
TeV J2032+4130	S45	-2.0 ± 0.6	1.5
	S46	-1.5 ± 0.3	1.1

NOTE—a: At the observed band at which is lower. The C factor of S8 and S9 is not lower than 1.5, which is a requirement for pulsar candidate (Frail et al. 2016).

flux densities between 20 and 350 mJy: S11, S32 and S42. Taking into account the spectral index errors involved, the remaining, S17, might be also included in the pulsar candidates group.

7. CONCLUSIONS

We have performed wide area two frequency radio observations of the rich Cygnus region with the GMRT. There are several HE/VHE sources with counterparts not known in this region and we searched for radio sources in the error ellipses of them to look for counterparts. We found several interesting radio sources within the error circle of the HE/VHE sources. The main conclusions are the following:

- In the error ellipses of 8 HE/VHE sources we detected 11 radio sources with very steep spectral index ($\alpha \leq -1.5$). Nine of them have a C-factor $\lesssim 1.5$, indicating that are pulsar candidates.
- Two sources, S40 and S46, show variability when compared to previous GMRT data at 610 MHz. Other sources (8), of which previous arcsec-resolution data were available, are steady whereas in 37 cases there is no previous data to compare.
- We have obtained a 325 MHz image of the supernova remnant Gamma-Cygni (G78.2+2.1) which contain 4FGL J2021.0+4031e and VER J2019+407. In a central region of 0.1 deg in size of 4FGL J2021.0+4031e we found no discrete radio sources.
- No radio sources were detected above 2 mJy level for 4FGL J2021.5+4026, 3FGL J2026.8+4003, 4FGL J2030.9+4416, 3FGL J2036.8+4234c and 4FGL J2038.4+4212. A radio source at 325 MHz was detected in the error ellipse of 3FGL J2039.4+4111.

The detection of radio sources with characteristics of pulsar candidates prompts for further investigation to confirm their nature, and from then on, to describe the extent to which they can contribute to the (very) high-energy sources. A follow-up study on timing of such sources with the Very Large Array, GMRT or VLBI facilities is needed to verify its nature. As quote Frail et al. (2016), such very high angular resolution is needed to discriminate resolved luminous high-redshift galaxies from unresolved pulsars.

ACKNOWLEDGMENTS

We thank the staff of the GMRT that made these observations possible. GMRT is run by the National Centre for Radio Astrophysics of the Tata Institute of Fundamental Research. We are also grateful to Josep Martí for useful comments. PB acknowledges support from ANPCyT PICT 0773–2017. CHIC acknowledges the support of the Department of Atomic Energy, Government of India, under the project 12-R&D-TFR-5.02-0700. JMP acknowledges financial support by the Spanish Ministerio de Economía, Industria y Competitividad (MINEICO/FEDER, UE) under grant AYA2016-76012-C3-1-P, from the State Agency for Research of the Spanish Ministry of Science and Innovation under grant PID2019-105510GB-C31 and through the “Unit of Excellence María de Maeztu 2020-2023” award to the Institute of Cosmos Sciences (CEX2019-000918-M), and by the Catalan DEC grant 2017 SGR 643. This research has made use of the SIMBAD and VizieR databases, operated at CDS, Strasbourg, France, and of NASA’s Astrophysics Data System bibliographic services.

APPENDIX

FIGURES OF THE RADIO SOURCES S1 TO S47

The ID of the radio source, the imaged band, and the contour levels with its unit are shown in each sub-figure.

REFERENCES

- Abdo, A. A., Allen, B. T., Aune, T., et al. 2009, *ApJL*, 700, L127, doi: [10.1088/0004-637X/700/2/L127](https://doi.org/10.1088/0004-637X/700/2/L127)
- Abdollahi, S., Acero, F., Ackermann, M., et al. 2020, *ApJS*, 247, 33, doi: [10.3847/1538-4365/ab6bcb](https://doi.org/10.3847/1538-4365/ab6bcb)
- Abeysekara, A. U., Archer, A., Aune, T., et al. 2018, *ApJ*, 861, 134, doi: [10.3847/1538-4357/aac4a2](https://doi.org/10.3847/1538-4357/aac4a2)
- Abeysekara, A. U., Albert, A., Alfaro, R., et al. 2020, *PhRvL*, 124, 021102, doi: [10.1103/PhysRevLett.124.021102](https://doi.org/10.1103/PhysRevLett.124.021102)
- Acero, F., Ackermann, M., Ajello, M., et al. 2015, *ApJS*, 218, 23, doi: [10.1088/0067-0049/218/2/23](https://doi.org/10.1088/0067-0049/218/2/23)
- Aharonian, F., Akhperjanian, A., Beilicke, M., et al. 2002, *A&A*, 393, L37, doi: [10.1051/0004-6361:20021171](https://doi.org/10.1051/0004-6361:20021171)
- . 2005, *A&A*, 431, 197, doi: [10.1051/0004-6361:20041552](https://doi.org/10.1051/0004-6361:20041552)
- Albert, J., Aliu, E., Anderhub, H., et al. 2008, *ApJL*, 675, L25, doi: [10.1086/529520](https://doi.org/10.1086/529520)
- Aliu, E., Archambault, S., Arlen, T., et al. 2013, *ApJ*, 770, 93, doi: [10.1088/0004-637X/770/2/93](https://doi.org/10.1088/0004-637X/770/2/93)
- Aliu, E., Aune, T., Behera, B., et al. 2014, *ApJ*, 783, 16, doi: [10.1088/0004-637X/783/1/16](https://doi.org/10.1088/0004-637X/783/1/16)
- Bartoli, B., Bernardini, P., Bi, X. J., et al. 2014, *ApJ*, 790, 152, doi: [10.1088/0004-637X/790/2/152](https://doi.org/10.1088/0004-637X/790/2/152)
- Bates, S. D., Lorimer, D. R., & Verbiest, J. P. W. 2013, *MNRAS*, 431, 1352, doi: [10.1093/mnras/stt257](https://doi.org/10.1093/mnras/stt257)
- Bednarek, W., & Bartosik, M. 2003, *A&A*, 405, 689, doi: [10.1051/0004-6361:20030593](https://doi.org/10.1051/0004-6361:20030593)
- Benaglia, P., De Becker, M., Ishwara-Chandra, C. H., Intema, H. T., & Isequilla, N. L. 2020a, *PASA*, 37, e030, doi: [10.1017/pasa.2020.21](https://doi.org/10.1017/pasa.2020.21)
- Benaglia, P., Ishwara-Chandra, C. H., Intema, H., Colazo, M. E., & Gaikwad, M. 2020b, *A&A*, 642, A136, doi: [10.1051/0004-6361/202037916](https://doi.org/10.1051/0004-6361/202037916)
- Bennett, C. L., Lawrence, C. R., Burke, B. F., Hewitt, J. N., & Mahoney, J. 1986, *ApJS*, 61, 1, doi: [10.1086/191108](https://doi.org/10.1086/191108)
- Biteau, J., & Williams, D. A. 2015, *ApJ*, 812, 60, doi: [10.1088/0004-637X/812/1/60](https://doi.org/10.1088/0004-637X/812/1/60)
- Bosch-Ramon, V., Romero, G. E., Araudo, A. T., & Paredes, J. M. 2010, *A&A*, 511, A8, doi: [10.1051/0004-6361/200913488](https://doi.org/10.1051/0004-6361/200913488)
- Camilo, F., Ray, P. S., Ransom, S. M., et al. 2009, *ApJ*, 705, 1, doi: [10.1088/0004-637X/705/1/1](https://doi.org/10.1088/0004-637X/705/1/1)
- Camilo, F., Kerr, M., Ray, P. S., et al. 2012, *ApJ*, 746, 39, doi: [10.1088/0004-637X/746/1/39](https://doi.org/10.1088/0004-637X/746/1/39)
- Capak, P. L., Teplitz, H. I., Brooke, T. Y., Laher, R., & Science Center, S. 2013, in *American Astronomical Society Meeting Abstracts*, Vol. 221, American Astronomical Society Meeting Abstracts #221, 340.06
- Chernyakova, M., Malyshev, D., Paizis, A., et al. 2019, *A&A*, 631, A177, doi: [10.1051/0004-6361/201936501](https://doi.org/10.1051/0004-6361/201936501)
- Cohen, M., Bieging, J. H., Dreher, J. W., & Welch, W. J. 1985, *ApJ*, 292, 249, doi: [10.1086/163154](https://doi.org/10.1086/163154)
- Condon, J. J., Cotton, W. D., Greisen, E. W., et al. 1998, *AJ*, 115, 1693, doi: [10.1086/300337](https://doi.org/10.1086/300337)
- Cutri, R. M., & al. 2012, *VizieR Online Data Catalog*, II/311
- Cutri, R. M., Skrutskie, M. F., van Dyk, S., et al. 2003, *VizieR Online Data Catalog*, II/246

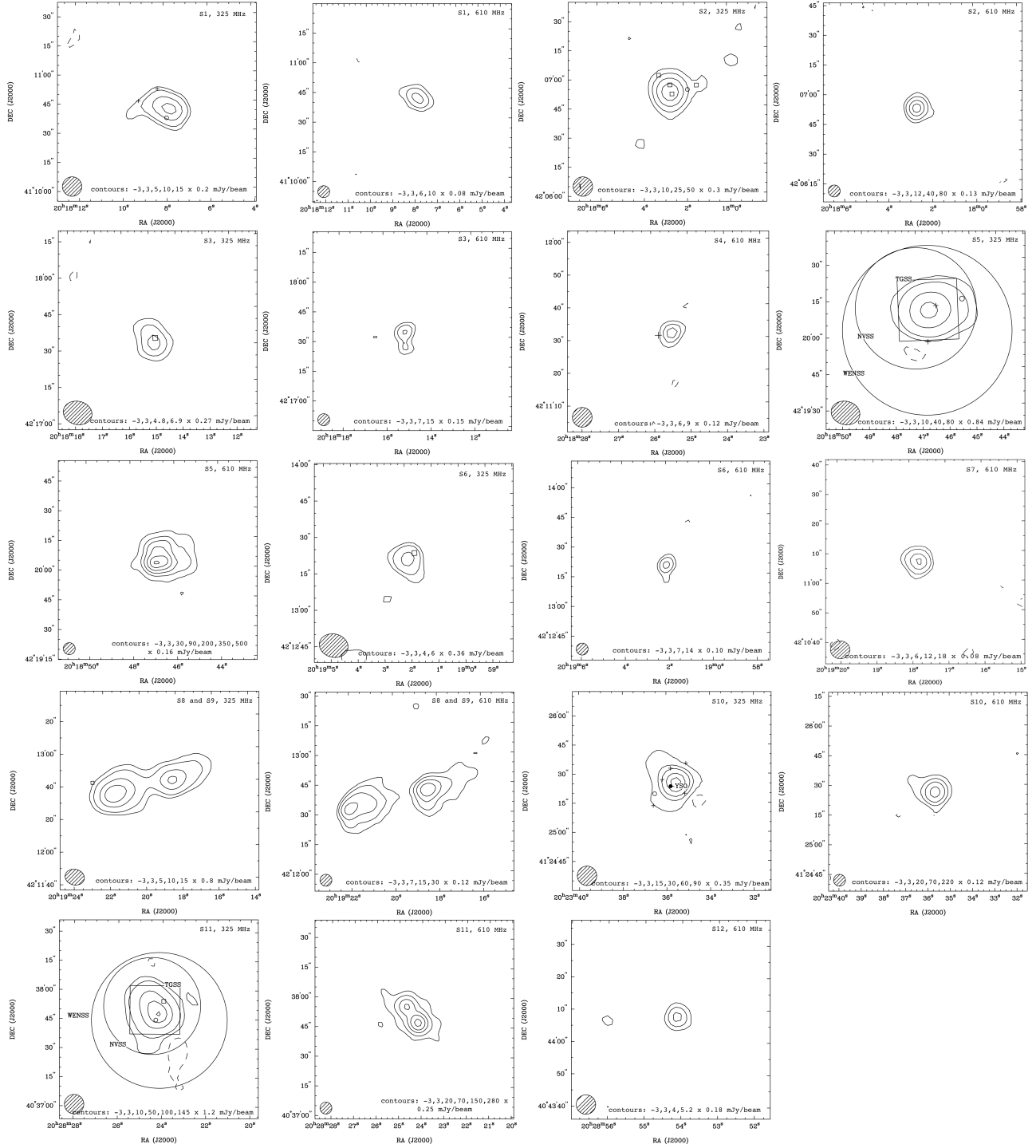


Figure 17. Figures of radio sources S1 to S12, at both observed frequency bands, except for S4, S7 and S12 which were only detected at 610 MHz. Counterparts found in the literature are also shown; the different symbols used are listed in Table 5, last column. For S12, the position of the YSO reported by [Kryukova et al. \(2014\)](#) is marked.

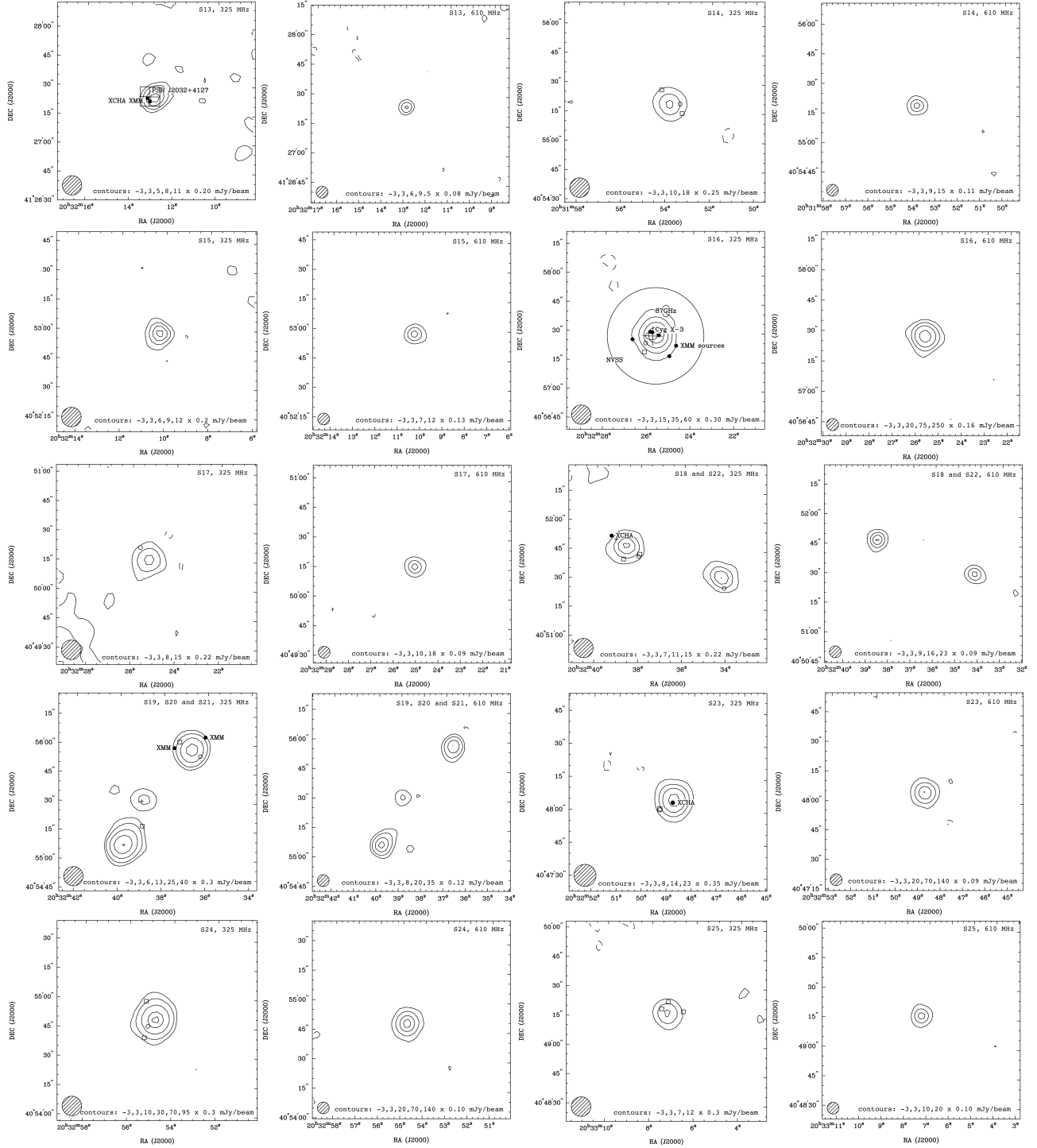


Figure 18. Figures of radio sources S13 to S25, at both observed frequency bands. Counterparts found in the literature are also shown; the different symbols used are listed in Table 5, last column. For S13, the box represents the source detected by [Paredes et al. \(2007\)](#), and the big cross that of the pulsar PSR J2032+4127. For S16, the big cross marks the position of Cyg X-3.

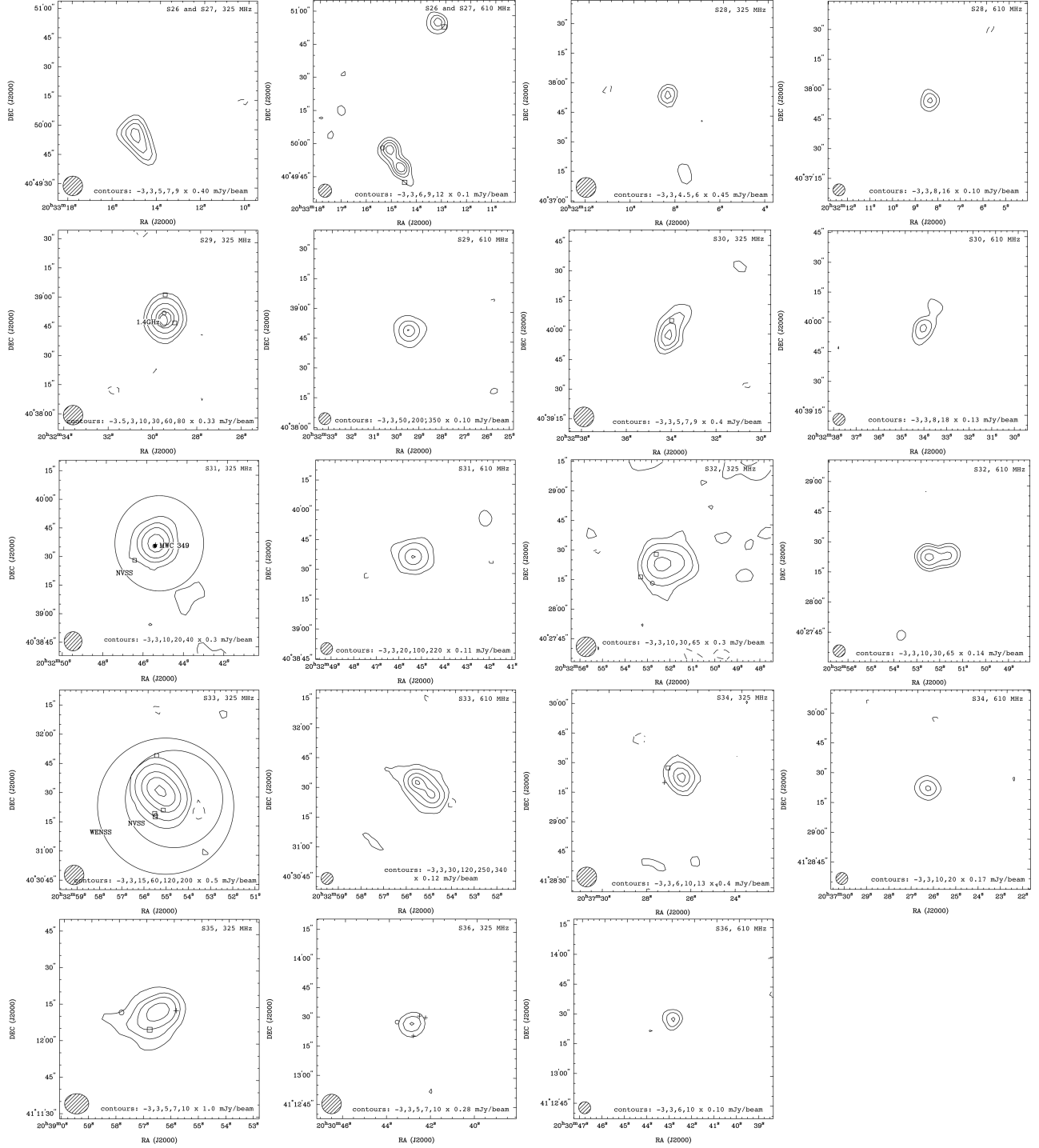


Figure 19. Figures of radio sources S26 to S36, at both observed frequency bands, except for S35 which was only observed at 325 MHz. Counterparts found in the literature are also shown; the different symbols used are listed in Table 5, last column.

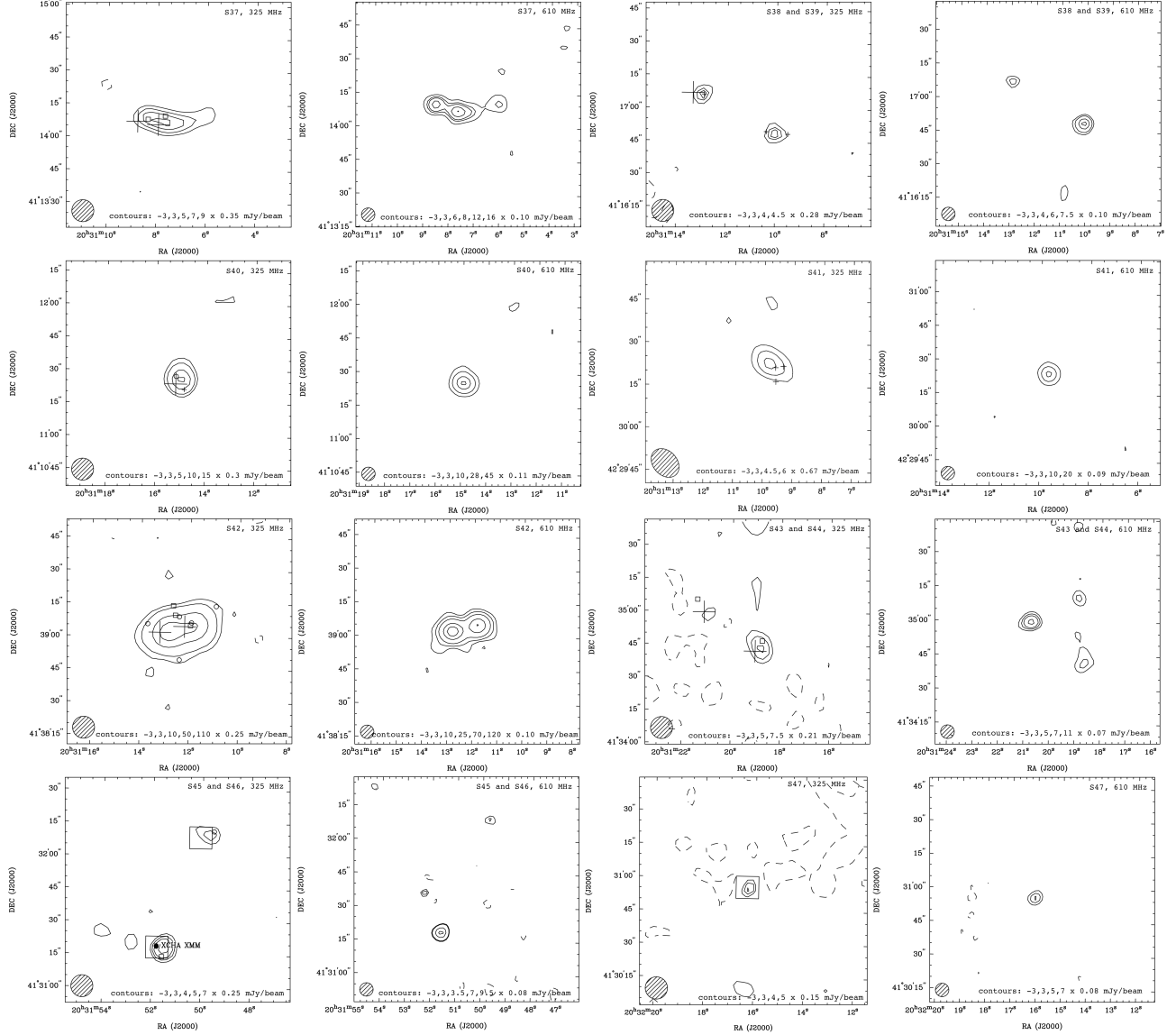


Figure 20. Figures of radio sources S37 to S47, at both observed frequency bands. Counterparts found in the literature are also shown; the different symbols used are listed in Table 5, last column. For S37, S39, S40, S42, S43 and S44, the big crosses mark the sources reported by [Martí et al. \(2007\)](#). For S45, S46 and S47, the boxes represents the source detected by [Paredes et al. \(2007\)](#).

- de Vries, M., & Romani, R. W. 2020, *ApJL*, 896, L7,
doi: [10.3847/2041-8213/ab9640](https://doi.org/10.3847/2041-8213/ab9640)
- Frail, D. A., Jagannathan, P., Mooley, K. P., & Intema, H. T. 2016, *ApJ*, 829, 119,
doi: [10.3847/0004-637X/829/2/119](https://doi.org/10.3847/0004-637X/829/2/119)
- Frail, D. A., Ray, P. S., Mooley, K. P., et al. 2018, *MNRAS*, 475, 942, doi: [10.1093/mnras/stx3281](https://doi.org/10.1093/mnras/stx3281)
- Gregory, P. C., & Condon, J. J. 1991, *ApJS*, 75, 1011,
doi: [10.1086/191559](https://doi.org/10.1086/191559)
- Hartman, R. C., Bertsch, D. L., Bloom, S. D., et al. 1999, *ApJS*, 123, 79, doi: [10.1086/313231](https://doi.org/10.1086/313231)
- Intema, H. T. 2014, SPAM: Source Peeling and Atmospheric Modeling. <http://ascl.net/1408.006>
- Intema, H. T., Jagannathan, P., Mooley, K. P., & Frail, D. A. 2017, *A&A*, 598, A78,
doi: [10.1051/0004-6361/201628536](https://doi.org/10.1051/0004-6361/201628536)
- Isequilla, N. L., Benaglia, P., Ishwara-Chandra, C. H., & Intema, H. 2020, *Boletín de la Asociación Argentina de Astronomía La Plata Argentina*, 61B, 124
- Ishwara-Chandra, C. H., Benaglia, P., De Becker, M., & Tej, A. 2019, *Bulletin de la Societe Royale des Sciences de Liege*, 88, 166
- Kryukova, E., Megeath, S. T., Hora, J. L., et al. 2014, *AJ*, 148, 11, doi: [10.1088/0004-6256/148/1/11](https://doi.org/10.1088/0004-6256/148/1/11)
- Ladouceur, Y., & Pineault, S. 2008, *A&A*, 490, 197,
doi: [10.1051/0004-6361:200810599](https://doi.org/10.1051/0004-6361:200810599)
- MAGIC Collaboration, Acciari, V. A., Ansoldi, S., et al. 2020, *arXiv e-prints*, arXiv:2010.15854.
<https://arxiv.org/abs/2010.15854>
- Mahy, L., Rauw, G., De Becker, M., Eenens, P., & Flores, C. A. 2013, *A&A*, 550, A27,
doi: [10.1051/0004-6361/201219425](https://doi.org/10.1051/0004-6361/201219425)
- Manchester, R. N., Hobbs, G. B., Teoh, A., & Hobbs, M. 2005, *AJ*, 129, 1993, doi: [10.1086/428488](https://doi.org/10.1086/428488)
- Martí, J., Luque-Escamilla, P. L., Paredes, J. M., et al. 2017, *A&A*, 598, A81, doi: [10.1051/0004-6361/201628863](https://doi.org/10.1051/0004-6361/201628863)
- Martí, J., Paredes, J. M., Ishwara Chandra, C. H., & Bosch-Ramon, V. 2007, *A&A*, 472, 557,
doi: [10.1051/0004-6361:20077712](https://doi.org/10.1051/0004-6361:20077712)
- Paredes, J. M., Ishwara-Chandra, C. H., Bosch-Ramon, V., et al. 2014, *A&A*, 561, A56,
doi: [10.1051/0004-6361/201322306](https://doi.org/10.1051/0004-6361/201322306)
- Paredes, J. M., Martí, J., Ishwara Chandra, C. H., & Bosch-Ramon, V. 2007, *ApJL*, 654, L135,
doi: [10.1086/511178](https://doi.org/10.1086/511178)
- Perley, R. A., & Butler, B. J. 2013, *ApJS*, 204, 19,
doi: [10.1088/0067-0049/204/2/19](https://doi.org/10.1088/0067-0049/204/2/19)
- Reipurth, B., & Schneider, N. 2008, *Star Formation and Young Clusters in Cygnus (ASP)*, 36
- Rengelink, R. B., Tang, Y., de Bruyn, A. G., et al. 1997, *A&AS*, 124, 259, doi: [10.1051/aas:1997358](https://doi.org/10.1051/aas:1997358)
- Sánchez-Sutil, J. R., Martí, J., Combi, J. A., et al. 2008, *A&A*, 479, 523, doi: [10.1051/0004-6361:20078498](https://doi.org/10.1051/0004-6361:20078498)
- Swanenburg, B. N., Bennett, K., Bignami, G. F., et al. 1981, *ApJL*, 243, L69, doi: [10.1086/183445](https://doi.org/10.1086/183445)
- Taylor, A. R., Goss, W. M., Coleman, P. H., van Leeuwen, J., & Wallace, B. J. 1996, *ApJS*, 107, 239,
doi: [10.1086/192363](https://doi.org/10.1086/192363)
- Uyaniker, B., Fürst, E., Reich, W., Aschenbach, B., & Wielebinski, R. 2001, *A&A*, 371, 675,
doi: [10.1051/0004-6361:20010387](https://doi.org/10.1051/0004-6361:20010387)
- Wang, S., Liu, J., Qiu, Y., et al. 2016, *VizieR Online Data Catalog*, J/ApJS/224/40
- Wendker, H. J., Higgs, L. A., & Landecker, T. L. 1991, *A&A*, 241, 551
- Zoonematkermani, S., Helfand, D. J., Becker, R. H., White, R. L., & Perley, R. A. 1990, *ApJS*, 74, 181,
doi: [10.1086/191496](https://doi.org/10.1086/191496)